MDPI

Article

Crystal Chemistry, Isomorphism, and Thermal Conversions of Extra-Framework Components in Sodalite-Group Minerals

Nikita V. Chukanov [1,2,*], Roman Yu. Shendrik [3], Marina F. Vigasina [2], Igor V. Pekov [2,4], Anatoly N. Sapozhnikov [3], Vasily D. Shcherbakov [2] and Dmitry A. Varlamov [1,5]

1. Institute of Problems of Chemical Physics, Russian Academy of Sciences, Chernogolovka, 142432 Moscow, Russia; dima@iem.ac.ru
2. Faculty of Geology, Moscow State University, 119991 Moscow, Russia; vigasina55@mail.ru (M.F.V.); igorpekov@mail.ru (I.V.P.); vasiliy7@gmail.com (V.D.S.)
3. Vinogradov Institute of Geochemistry, Siberian Branch of Russian Academy of Sciences, 664033 Irkutsk, Russia; roshen@yandex.ru (R.Y.S.); sapozh@igc.irk.ru (A.N.S.)
4. Vernadsky Institute of Geochemistry and Analytical Chemistry, Russian Academy of Sciences, 119991 Moscow, Russia
5. Institute of Experimental Mineralogy RAS, Chernogolovka, 142432 Moscow, Russia
* Correspondence: chukanov@icp.ac.ru

Abstract: Isomorphic substitutions of extra-framework components in sodalite-group aluminosilicate minerals and their thermal conversions have been investigated using infrared, Raman, electron spin resonance (ESR), as well as ultraviolet, visible and near infrared (UV–Vis–near IR) absorption spectroscopy methods and involving chemical and X-ray diffraction data. Sodalite-related minerals from gem lazurite deposits (haüyne, lazurite, and slyudyankaite) are characterized by wide variations in S-bearing extra-framework components including SO_4^{2-} and various polysulfide groups ($S_2^{\bullet-}$, $S_3^{\bullet-}$, $S_4^{\bullet-}$ radical anions, and S_4 and S_6 neutral molecules) as well as the presence of CO_2 molecules. Heating at 700 °C under reducing conditions results in the transformation of initial S-bearing groups SO_4^{2-} and $S_3^{\bullet-}$ to a mixture of S^{2-}, HS^-, $S_2^{\bullet-}$, and $S_4^{\bullet-}$ and transformation of CO_2 to a mixture of CO_3^{2-} and $C_2O_4^{2-}$ or $HC_2O_4^-$ anionic groups. Further heating at 800 °C in air results in the decomposition of carbonate and oxalate groups, restoration of the SO_4^{2-} and $S_3^{\bullet-}$ groups, and a sharp transformation of the framework. The HS^- anion is stable only under reducing conditions, whereas the $S_3^{\bullet-}$ radical anion is the most stable polysulfide group. The HS^--dominant sodalite-group mineral sapozhnikovite forms a wide solid-solution series with sodalite. The conditions required for the formation of HS^-- and $CO_2{}^0$-bearing sodalite-group minerals are discussed.

Keywords: sodalite group; isomorphism; solid solutions; infrared spectroscopy; electron (UV-Vis) spectroscopy; Raman spectroscopy; electron spin resonance; photoluminescence

1. Introduction

Minerals belonging to the sodalite group are microporous cubic or pseudo-cubic alumino- and beryllosilicates which occur in different kinds of alkaline magmatic and metasomatic rocks. Some of them (sodalite, haüyne, and nosean) belong to important rock-forming minerals.

The unit cell parameters of the "idealized sodalite (**SOD**-type) framework" deposited in the Database of Zeolite Structures are a = 8.9561 Å; V = 718.4 Å^3; and space group Im-3m (aristotype) [1,2]. However, due to different schemes of the Si/Al ordering as well as specific features of the occupation of the intra-framework cavities (sodalite cages) by extra-framework components, the observed symmetry is usually lower. A distinctive feature of sodalite-type compounds is a three-dimensional system of channels consisting of sodalite cages and running along different directions. The extra-framework constituents in sodalite-group minerals are more diverse than in the members of the related cancrinite

group and include different cations (Na^+, $[N(CH_3)_4]^+$, Ca^{2+}, Mn^{2+}, Fe^{2+}, and Zn^{2+}), anions (Cl^-, F^-, OH^-, HS^-, S^{2-}, and SO_4^{2-}), radical anions ($S_3^{\bullet-}$), and neutral molecules (H_2O, CO_2, S_6) as species-defining components. Some subordinate, admixed components (K^+, H^+, $S_2^{\bullet-}$, $S_4^{\bullet-}$, $SO_4^{\bullet2-}$, S_3, S_4, MoO_4^{2-}, WO_4^{2-}, AsO_4^{3-}, and COS) were identified in sodalite-group minerals using a multianalytical approach involving different spectroscopic methods [3–6].

To date, many dozens of chemically different microporous compounds with the **SOD**-type framework have been synthesized. Interest in such compounds is caused by their specific properties, which make it possible to consider them as advanced materials with technologically important properties. The hydrothermal method was applied to obtain sodalite-type compounds with aluminosilicate frameworks as well as frameworks containing W-, Mo-, Ga-, Be-, Ge-, P-, or As-centered tetrahedra, with a wide variety of extra-framework cations and anions [7]. Microporous compounds belonging to the topological type of sodalite are advanced materials that can be used as pigments, sorbents for water purification and gas sorption, matrices for immobilization of radioactive isotopes and heavy metals, hydrogen and methane storage, superconductors, catalysts, membranes for separation of gases and desalination of seawater, etc. [8–37].

This paper provides new data on the isomorphism of extra-framework components in some sodalite-group minerals as well as mechanisms for their thermal conversions.

2. Materials and Methods

The studied samples are listed below. Their empirical formulae are partly taken from literature sources. Chemical data for newly analyzed samples are given in Table 1. Samples 1–6 and 9 were collected at the Malo-Bystrinskoe gem lazurite deposit, Baikal Lake area, Siberia, Russia.

Table 1. Chemical composition (wt.%) of haüyne from the Malo-Bystrinskoe gem lazurite deposit, Baikal Lake area, Siberia, Russia obtained in this work. Representative chemical analyses of sodalite–sapozhnikovite series minerals (Sample 12) from Karnasurt Mt., Lovozero massif, Kola Peninsula, Russia obtained in this work.

Sample No.	1	2
Color	Bluish lilac	Deep blue
Na_2O	18.04	17.92
K_2O	0.21	0.74
CaO	7.83	7.60
Al_2O_3	28.63	27.79
Fe_2O_3	0	0.19
SiO_2	33.65	33.46
CO_2 [a]	0.67	0.25
SO_3 [b]	14.58	15.33
F	0.42	0
Cl	0.32	0.31
$-O=Cl,F$	-0.25	-0.07
Total	104.10	103.52

Analysis No.	1	2	3	4	5	6	7	8
				Contents, wt. %				
Na_2O	23.60	24.20	24.60	24.28	24.49	24.34	24.01	24.21

Table 1. *Cont.*

Sample No.				1			2	
Al_2O_3	30.84	31.50	31.37	31.38	31.69	31.29	31.16	31.33
Fe_2O_3	0.36	-	0.27	-	-	0.13	-	-
SiO_2	36.03	36.88	36.95	36.61	36.82	36.50	36.48	36.26
HS *	2.78	3.10	3.52	3.74	4.17	4.48	4.86	5.27
Cl	3.97	3.41	3.32	3.07	2.68	2.31	1.85	1.35
–O=(Cl,HS)	–1.57	–1.52	–1.60	–1.59	–1.61	–1.60	–1.60	–1.58
Total	96.01	97.57	98.43	97.49	98.24	97.45	96.76	96.84
Formula Calculated on the Basis of Al + Fe + Si = 12 Atoms Per Formula Unit								
Na	7.56	7.61	7.72	7.68	7.68	7.71	7.56	7.70
Al	6.00	6.02	5.99	6.03	6.04	6.02	6.02	6.05
Fe	0.04	-	0.03	-	-	0.02	-	-
Si	5.96	5.98	5.98	5.97	5.96	5.96	5.98	5.95
S	0.84	0.91	1.03	1.11	1.22	1.33	1.45	1.57
Cl	1.11	1.06	0.91	0.85	0.73	0.64	0.51	0.38
S + Cl	1.95	1.97	1.94	1.96	1.95	1.97	1.96	1.95

[a] CO_2 contents corresponding to CO_2 molecules were determined from the IR spectra using a procedure described in [3]; [b] All sulfur is given as SO_3, which results in high total sums for the samples bearing sulfide groups. * Recalculated from values for S measured by electron microprobe. Dash means Fe content below detection limit. Analyses are ordered by increase of the S: Cl ratio.

Sample 1 is bluish lilac S_4-bearing haüyne. The mineral forms granular aggregate (4 cm across) embedded in calciphyre. The associated minerals are calcite, diopside, and pyrite. The charge-balanced empirical formula is (Table 1; the contents of CO_2 and HS^- were estimated from the IR spectrum; for the identification of H_2S and S_4, see below): $Na_{6.24}Ca_{1.49}K_{0.05}(Si_{5.99}Al_{6.01}O_{24})(SO_4)_{1.50}(H_2S)_{0.075}(S_4)_{0.09}Cl_{0.10}F_{0.24}(CO_2)_{0.16} \cdot nH_2O$ (Z = 1).

Sample 2 is deep blue haüyne. It forms single-crystal grains up to 1 cm across in association with calcite, phlogopite, and accessory sphalerite, Zn-bearing spinel, and grossular. The empirical formula of Sample 2 is (Table 1): $Na_{6.28}Ca_{1.47}K_{0.17}(Si_{6.05}Al_{5.92}Fe_{0.03}O_{24})(SO_4^{2-})_{1.68} S^0_{0.40}Cl_{0.06}(CO_2)_{0.06} \cdot nH_2O$, where S^0 is all sulfide sulfur provided that it occurs in neutral molecules.

Sample 3 is lilac haüyne forming a rim around light gray fine-grained aggregates of earlier silicates up to 2 cm across. The associated minerals are lazurite, sodalite, diopside, and calcite. The empirical formula is $Na_{6.39}K_{0.06}Ca_{1.57}(Si_{6.08}Al_{5.92}O_{24})(SO_4)_{1.78}(S_4)_{0.03}(S^{2-})_{0.02}Cl_{0.07}(CO_2)_{0.15} \cdot nH_2O$ (Z = 1) [4]. The mineral is cubic, with the unit cell parameter a = 9.076 Å.

Sample 4 is light blue $SO_3^{\bullet-}$-bearing haüyne with the empirical formula $Na_{6.45}K_{0.03}Ca_{1.35}(Si_{6.07}Al_{5.93}O_{24})(SO_4)_{1.35}(SO_3^{\bullet-})_{1.35}S_2^{\bullet-}{}_{0.02}Cl_{0.16}(CO_2)_{0.02} \cdot nH_2O$ (Z = 1) [4]. The unit cell parameter is a = 9.067 Å. The mineral forms grains up to 5 mm in calciphyre, in association with pyrite.

Sample 5 is bright blue haüyne with the empirical formula $Na_{6.45}K_{0.01}Ca_{1.36}(Si_{6.06}Al_{5.94}O_{24})(SO_4)_{1.58}S^0_{0.43}Cl_{0.09}(CO_2)_{0.02} \cdot nH_2O$, where S^0 is all sulfide sulfur provided that it occurs in neutral molecules. The unit cell parameter is a = 9.071 Å. The mineral forms grains in coarse-grained calciphyre consisting mainly of calcite, with subordinate diopside.

Sample 6 is the holotype specimen of slyudyankaite $Na_{28}Ca_4(Si_{24}Al_{24}O_{96})(SO_4)_6(S_6)_{1/3}(CO_2) \cdot 2H_2O$ [38]. The mineral is triclinic, space group: $P1$, a = 9.0523 (4) Å, b = 12.8806 (6) Å, c = 25.681 (1) Å, α = 89.988(2)°, β = 90.052(1)°, γ = 90.221(1)°, and V = 2994.4 (2) Å³. The empirical formula is $Na_{27.57}Ca_{4.05}K_{0.11}(Si_{24.52}Al_{23.48}O_{96})(SO_4)_{6.06}S^0_{2.42}Cl_{0.12}(CO_2)_{1.43} \cdot 2.21H_2O$ (Z = 1), where $S^0_{2.42}$ is total sulfide sulfur, mainly occurring as S_6 and subordinate S_4 neutral

molecules, according to the structural data. The color of slyudyankaite is nonuniform: from blue-green in the major part of grains to pink and yellow in thin peripheral zones. The mineral forms isolated anhedral equant grains up to 0.5 cm across. The associated minerals are diopside, calcite, fluorapatite, phlogopite, lazurite, and pyrite.

Sample 7 is gray nosean forming crystals up to 0.5 cm across and elongate twins on (111) up to 1 cm long in cavities of nosean sanidinite. The sample originates from the In den Dellen (Zieglowski) pumice quarry, 1.5 km NE of Mendig, Laach Lake (Laacher See) paleovolcano, Eifel region, Rhineland-Palatinate, Germany. The associated minerals are sanidine, augite, annite, and zircon. The empirical formula of Sample 7 is [3]: $(H_3O)_x Na_{5.72} K_{0.64} Ca_{0.33} (Si_{6.43} Al_{5.51} Fe_{0.06} O_{24})(SO_4)_{1.21} Cl_{0.11} F_{0.09} (CO_2)_{0.11} \cdot n H_2O$ (Z = 1).

Sample 8 is the holotype specimen of sapozhnikovite $Na_8(Al_6Si_6O_{24})(HS)_2$ from a hydrothermally altered urtite-like rock at Karnasurt Mountain, Lovozero alkaline massif, Kola Peninsula, Russia [39]. The mineral forms isolated colourless to pale grayish anhedral equant grains up to 0.5 cm across. The empirical formula is $Na_{7.73} Al_{6.08} Si_{5.97} O_{24} (HS)_{1.25}$ $Cl_{0.60} \cdot 0.16 H_2O$ (Z = 1). Sapozhnikovite is cubic, $P\bar{4}3n$, with a = 8.91462(7) Å.

Sample 9 is the neotype specimen of lazurite with the empirical formula $(Na_{6.97} Ca_{0.88}$ $K_{0.10})_{7.96} (Si_{6.04} Al_{5.96} O_{24})(SO_4)_{1.09} (S_3^{\bullet-})_{0.55} S^{2-}_{0.05} Cl_{0.04} \cdot 0.72 H_2O$ [5]. The associated minerals are calcite and diopside as well as accessory dolomite, forsterite, and phlogopite. The crystal structure of Sample 9 is characterized by commensurate and incommensurate modulations; the a parameter of the cubic sub-cell is equal to 9.087(3) Å.

Sample 10 is the holotype specimen of the recently IMA-approved new F-dominant sodalite-group mineral bolotinaite (IMA 2021-088). The mineral occurs as isolated yellow elongate interpenetration twins up to 1 mm long in cavities of a volcanic ejectum of trachitoid sanidinite collected in the In den Dellen pumice quarry, Eifel region, Rhineland-Palatinate, Germany. The associated minerals are sanidine, nepheline, annite, and zircon. The empirical formula of Sample 10 is $(Na_{5.92} K_{0.82} Ca_{0.10} H_{0.08})(Si_{6.33} Al_{5.67} O_{24})(SO_4)_{0.17} F_{0.84}$ $Cl_{0.16} (CO_2)_{0.38} \cdot 3.96 H_2O$.

Sample 11 is blue sodalite forming grains up to 3 cm across in a cancrinite-sodalite pegmatite uncovered at the western slope of Mount Kobelikha, Vishnevye Gory, Vishnevogorskiy syenite-miaskite complex, South Urals, Russia. The associated minerals are potassic feldspar, cancrinite, annite, muscovite, different zeolites, as well as accessory zircon, thorite, ilmenite, columbite-(Fe), Nb-bearing rutile, a pyrochlore-group mineral, various sulfides, etc. The composition of Sample 10 is close to the end-member formula $Na_8(Si_6Al_6O_{24})Cl_2$ [3].

Sample 12 was collected from the same area as sapozhnikovite (Sample 8), north slope of Karnasurt Mountain located in the northern part of the Lovozero alkaline massif. This sample includes several similar but not identical to each other pieces of hydrothermally altered highly agpaitic urtite-like rocks containing rock-forming minerals of the sodalite–sapozhnikovite solid-solution series. Their share in a rock varies from 5 to 20 vol.%. Other rock-forming minerals are nepheline (the major constituent: >60 vol.%), aegirine, albite, potassic feldspar, natrolite, and kyanoxalite in different proportions; accessory minerals are murmanite (sometimes with lomonosovite relics), fluorapatite, and loparite-(Ce). Sodalite–sapozhnikovite series minerals form white or colourless, with strong orange fluorescence in longwave UV light (λ = 330 nm), grains up to 1 cm across. The representative chemical compositions of these minerals are given in Table 1.

Chemical analyses of haüyne Samples 1 and 2 (Table 1) were carried out using a Tescan VEGA-II XMU INCA Energy 450 (TESCAN, Brno, Czech Republic) (EDS mode, 20 kV, 120–150 pA, beam size 120 nm, excitation zone < 5 μm). The following standards were used: CaF_2 for F, albite for Na, synthetic Al_2O_3 for Al, wollastonite for Ca, potassium feldspar for K, SiO_2 for Si, Fe metal for Fe, and FeS_2 for S. Chemical analyses of sodalite–sapozhnikovite series minerals (Sample 12, Table 1) were carried out using a Jeol JSM-6480LV scanning electron microscope equipped with an INCA-Wave 500 wavelength-dispersive spectrometer (Laboratory of Analytical Techniques of High Spatial Resolution, Department of Petrology, Geological Faculty, Moscow State University), with an acceleration voltage of 20 kV, a beam

current of 10 nA, and a 10 μm beam diameter. The standards used are as follows: jadeite for Na, Al and Si, FeS_2 for Fe, ZnS for S, and NaCl for Cl. Contents of other elements with atomic numbers >6 are below detection limits.

Additionally, chemical compositions of 55 samples of minerals belonging to the sodalite–sapozhnikovite solution series were investigated.

The diffuse absorption spectra in the near infrared, visible, and ultraviolet (NIR/Vis/UV) ranges were measured at room temperature using a Lambda 950 spectrophotometer (Perkin-Elmer, Shelton, CT, USA). In particular, the absorption spectra of platelets of Sample 1 (about 1 mm thick) were measured in the transmission mode through a circular diaphragm 0.8 mm in diameter. The spectra were measured in an integrating sphere at room temperature. To do this, small crystals of the studied mineral were placed in a quartz test tube, transparent in the region of 250–2000 nm, and the test tube was placed in an integrating sphere.

The ESR spectra were measured with a RE-1306 X-band spectrometer (KBST, Smolensk, Russia) with a frequency of 9.3841 GHz at room temperature and 9.1841 GHz at 77 K. For low-temperature measurements, a quartz ampoule with the sample was placed in a flooded cryostat.

Heating of Samples 3 and 4 was carried out according to the following scheme. The samples were placed in a muffle furnace in air and sequentially heated every 50 °C for 10 min. After holding at each of the temperatures, ESR and NIR/Vis/UV diffuse absorption spectra were measured.

Thermal conversions of other studied samples were carried out in two stages. In the first stage, the samples were heated for three days at 700 °C in reducing atmosphere (over the Fe-FeS buffer). Thereafter, parts of the preheated samples were annealed at 800 °C in air for 24–36 h.

The powder X-ray diffraction study was carried out at room temperature with an automatic powder diffractometer (D8 ADVANCE, Bruker, Germany) equipped with a Göbel mirror. The powder X-ray diffraction patterns were obtained in step scan mode (in the 2θ range of 10 to 80°) using CuKα radiation at an accelerating voltage of 40 kV, with a current of 40 mA, time per step of 1 s, and a 2θ step of 0.02°. Calculations of interplanar distances were performed using the software that was delivered with the diffractometer (DIFFRAC Plus Evaluation package EVA, Bruker AXS, Bruker, Germany). Unit cell parameters were refined using the (440), (611), (622), and (721) reflections.

3. Results

3.1. Isomorphism of Extra-Framework Components in Cubic Sodalite-Group Minerals

Raman spectra are very sensitive to anionic groups and neutral molecules containing sulfide sulfur. Representative Raman spectra of cubic sodalite-group minerals are given in Figures 1–3.

The assignment of bands in the Raman spectra of cubic sodalite-group minerals shown in Figures 1–3 (Table 2) was made in accordance with [3,4,38–50].

Except for a very weak band at 285 cm^{-1} (combination of low–frequency lattice modes involving Na$^+$ cations), all bands in the Raman spectrum of lazurite (Sample 9: curve *b* in Figure 1) correspond to the $S_3^{\bullet-}$ radical anion [5]. Weak bands of sulfate groups are not observed in the Raman spectrum of Sample 9 because of their overlapping with the bands of $S_3^{\bullet-}$.

Analogous bands of the trisulfide radical anion are present in the spectrum of bluish lilac haüyne (Sample 1), which contains trace amounts of $S_3^{\bullet-}$ (curve *a* in Figure 1). Additionally, in the Raman spectrum of Sample 1, bands of SO_4^{2-} groups are observed at 987 cm^{-1} [symmetric stretching vibrations, $A_1(\nu_1)$ mode], 616 cm^{-1} [bending vibrations, $F_2(\nu_4)$ mode], and 442 cm^{-1} [bending vibrations, the $E(\nu_2)$ mode]. A series of distinct Raman bands (at 327, 650, and 682 cm^{-1}) corresponding to S_4 molecules having *cis-*, *gahche-* and *trans-*conformations, respectively, as well as bands of carbonate groups (at 1953 and 1460 cm^{-1}), H_2S molecules (at 2580 cm^{-1}), and hydronium cations H_3O^+ (at 3005 and 3280 cm^{-1}) (Table 2) are the specific feature of Sample 1 distinguishing it from all other

haüyne samples studied in this work and elsewhere [1,2,48]. The presence of hydronium in Sample 1 is in agreement with the deficit of extra-framework cations determined by the electron microprobe analysis (Table 1).
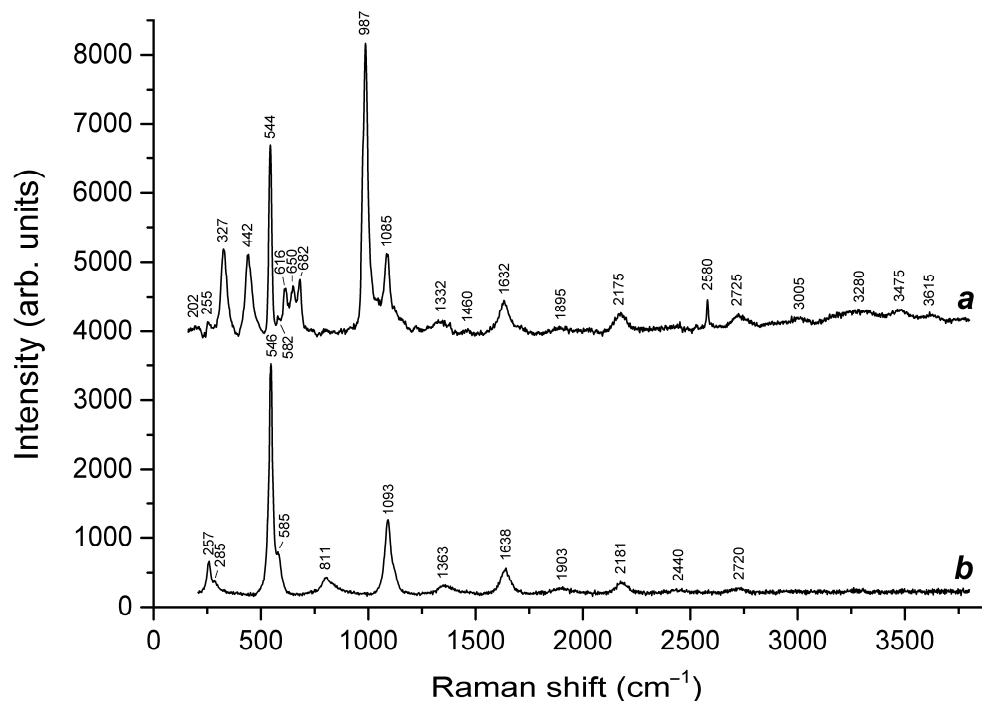

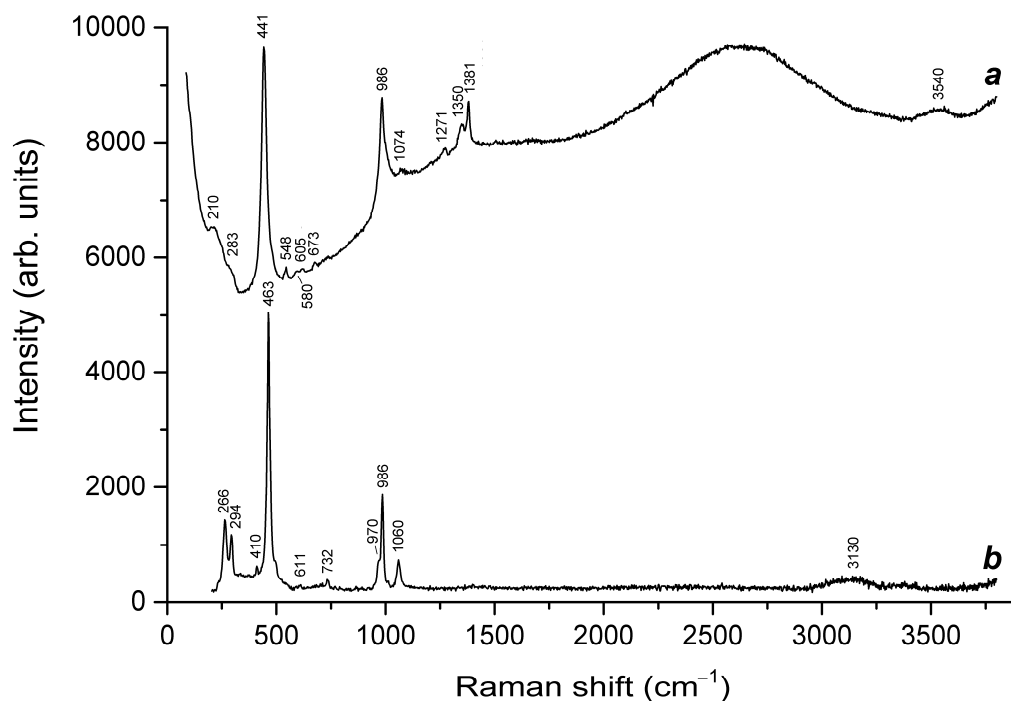**Figure 1.** Raman spectra of (**a**) S_4-bearing haüyne (Sample 1) and (**b**) lazurite (Sample 9).

Figure 2. Raman spectra of (**a**) bolotinaite (Sample 10) and (**b**) sodalite (Sample 11).
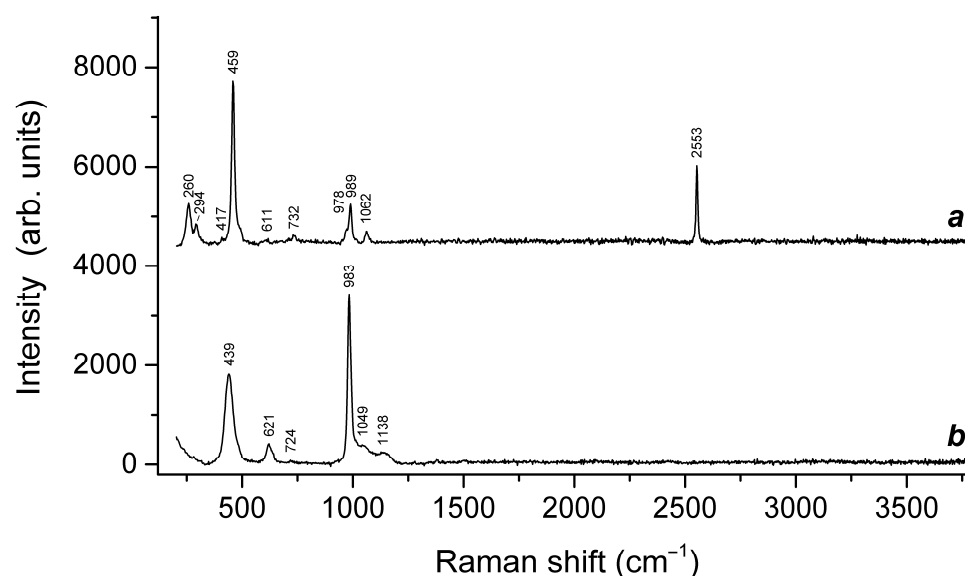
Figure 3. Raman spectra of (**a**) sapozhnikovite (Sample 8) and (**b**) nosean (Sample 7).

Table 2. Assignment of Raman bands of cubic sodalite-group minerals.

Raman Shift (cm^{-1})						Assignment
Sample No.						
1	**7**	**8**	**9**	**10**	**11**	
202w	-	-	-	210	-	Combination of low-frequency lattice modes and/or *trans*-S$_4$ bending mode
255	-	257	-	-	-	S$_3^{\bullet-}$ bending mode (ν_2)
-	-	260	-	-	266	Bending vibrations of the [ClNa$_4$]$^{3+}$ and [(HS)Na$_4$]$^{3+}$ clusters
-	-	294	285w	283w	-	Combination of low–frequency lattice modes involving Na$^+$ cations and/or S$_6$ bending mode
327	-	-	-	-	-	*cis*-S$_4$ mixed (bending + stretching) ν_4 mode
-	-	417w	-	-	410w	Bending vibrations of the aluminosilicate framework
442	439		-	441s	-	SO$_4^{2-}$ [the *E*(ν_2) mode] and/or δ[O–Si(Al)–O] bending vibrations
-	-	459s	-	-	463s	Stretching vibrations of the [ClNa$_4$] and [(HS)Na$_4$] clusters
544s	-	-	546s	548w	-	S$_3^{\bullet-}$ symmetric stretching (ν_1) mode
582w	-	-	585	-	-	S$_3^{\bullet-}$ antisymmetric stretching (ν_3), possibly, overlapping with the stretching band of S$_2^{\bullet-}$
-	-	-	-	580w, 605w	-	S$_2^{\bullet-}$ stretching mode
-	-	611w	-	-	611w	Overtone of vibrations involving Na$^+$ cations?
616	621	-	-	-	-	SO$_4^{2-}$ bending vibrations [*F*$_2$(ν_4) mode]
650	-	-	-	-	-	*gauche*-S$_4$ symmetric stretching A$_1$(ν_1) mode
682	-	-	-	673w	-	*trans*-S$_4$ symmetric stretching ν_3 mode
-	724w	732w	-	-	732w	Mixed vibrations of the aluminosilicate framework

Table 2. *Cont.*

| Raman Shift (cm^{-1})						Assignment
Sample No.						
1	**7**	**8**	**9**	**10**	**11**	
987s	983s	978, 989	-	986s	970, 986	SO_4^{2-} symmetric stretching vibrations [$A_1(\nu_1)$ mode]
1053w	1049	1062	-	-	1060	Stretching vibrations of the framework and/or CO_3^{2-} symmetric stretching vibrations
-	-	-	-	1074	-	HF libration
1085	-	-	1093s	-	-	$S_3^{\bullet-}$ overtone ($2 \times \nu_1$)
-	1138	-	-	-	-	SO_4^{2-} asymmetric stretching vibrations [$F_2(\nu_3)$ mode], possibly, overlapping with $S_2^{\bullet-}$ overtone ($2 \times \nu_1$)
-	-	-	-	1271	-	CO_2 Fermi resonance
1332	-	-	-	-	-	Overtone of the *cis*-S_4 antisymmetric stretching mode ($2 \times \nu_3$)
-	-	-	-	1350	-	H^+ translation
-	-	-	1363	-	-	$S_3^{\bullet-}$ combination mode ($2\nu_1 + \nu_2$)
-	-	-	-	1381	-	CO_2 Fermi resonance
1460w	-	-	-	-	-	CO_3 asymmetric stretching mode
1632	-	-	1638	-	-	$S_3^{\bullet-}$ overtone ($3 \times \nu_1$)
1895	-	-	-	-	-	$S_3^{\bullet-}$ combination mode ($3 \times \nu_2 + \nu_1$)
2175	-	-	2181	-	-	$S_3^{\bullet-}$ overtone ($4 \times \nu_1$)
-	-	-	2440w	-	-	$S_3^{\bullet-}$ combination mode ($4 \times \nu_2 + \nu_1$)
-	-	2553	-	-	-	HS^- stretching mode
2580	-	-	-	-	-	H_2S symmetric stretching mode
2725	-	-	2720	-	-	$S_3^{\bullet-}$ overtone ($5 \times \nu_1$)
3005, 3280	-	-	-	-	3130	H_3O^+ stretching mode
3475, 3615	-	-	-	3540	-	H_2O stretching vibrations

Ideally, sodalite, bolotinaite and sapozhnikovite are the end-members of the solid-solution system with the general formula [$Na_7(\square,Na)$]($Si_6Al_6O_{24}$){$Cl,HS,[F_{0.5}(H_2O)_2]$}$_2$. However, natural samples of these minerals contain various extra-framework impurities (K, H_3O^+, SO_4^{2-}, $S_2^{\bullet-}$, CO_2, S_4, HF, etc.) The Raman spectrum of sapozhnikovite in the range of 200–2500 cm^{-1} is very close to the spectrum of typical sodalite (Figures 2 and 3). The only significant distinctive feature of sapozhnikovite is a strong Raman band at 2553 cm^{-1} corresponding to stretching vibrations of HS^- anions. Bolotinaite is the member of this solid-solution system most enriched in impurities (Table 1). In particular, it contains $S_2^{\bullet-}$, which is the cause of the yellow color of this mineral and its strong luminescence under laser beams (Figure 2).

In the NIR/Vis/UV absorption spectrum of Sample 1, strong bands with the maxima at 0.65, 0.88, 2.05, and 2.38 eV (respectively, 1900, 1400, 605, and 520 nm) as well as absorption growth above 2.7 eV (460 nm) and a weak band at 1.33 eV (920 nm) are observed (Figure 4). The ESR spectrum of Sample 1 contains a sextet of Mn^{2+} ions in the low-spin state (S = $^1/_2$ [51]) with g = 2.001, a strong single band with g = 2.002, and a weak band with g = 2.036 (Figure 5). Most probably, Mn^{2+} ions occur in calcite forming inclusions in haüyne individuals.
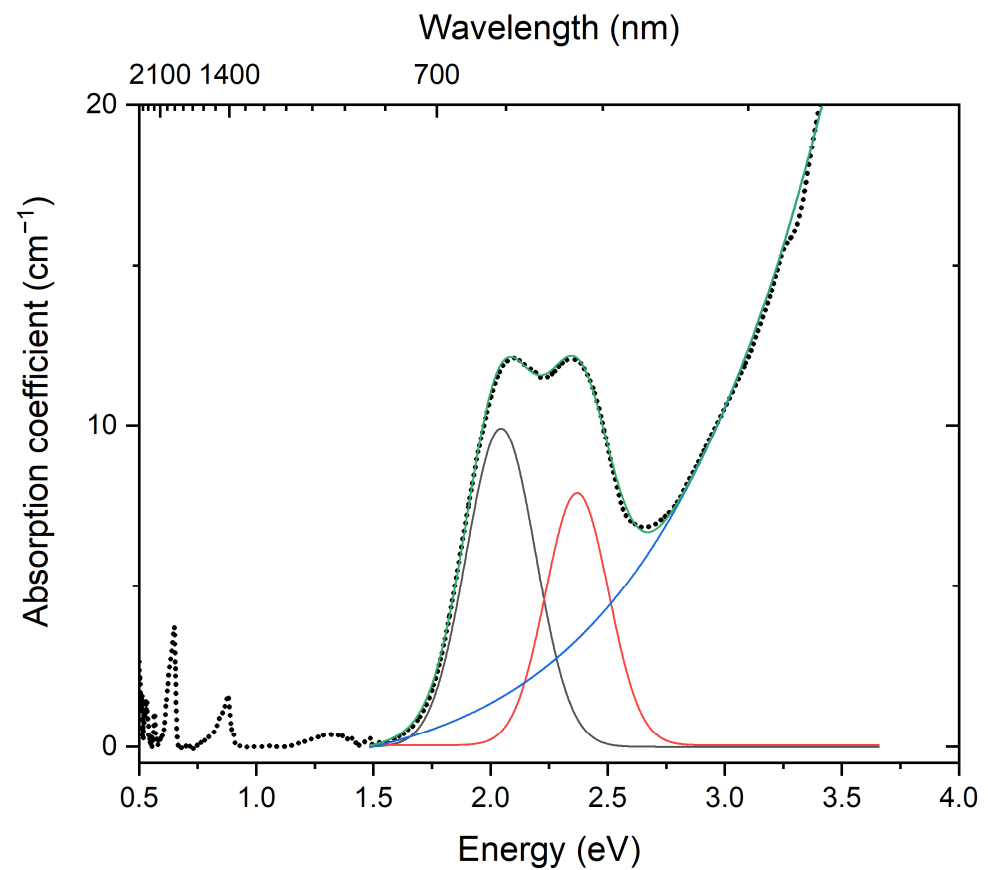
Figure 4. Absorption spectrum of haüyne (Sample 1, dotted curve). The black and red solid lines show the deconvolution of the doublet in the region of 2.0–2.5 eV into two peaks, and the total decomposition curve is shown with green color.
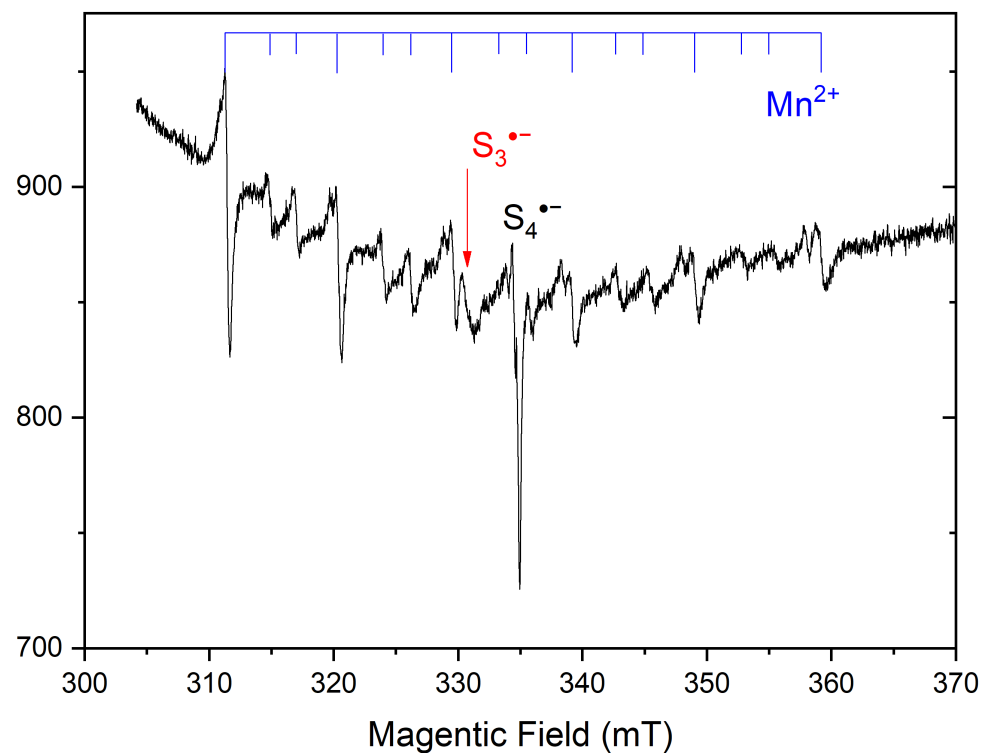
Figure 5. ESR spectrum of haüyne (Sample 1) measured at room temperature.

The absorption bands with maxima at 0.65 and 0.88 eV are associated with the vibrational modes of water in the studied mineral. The absorption bands with maxima at 2.05 and 2.38 eV, which impart a blue color to the studied mineral, can be associated with the presence of $S_3^{\bullet-}$ radical anions, which are easily detected by ESR [4,5], while the lilac hue can be associated with the presence of S_4 molecules (red chromophore). In the samples under study, the ESR signal characteristic of $S_3^{\bullet-}$ (with $g = 2.036$) is practically not observed, which indicates a very low concentration of $S_3^{\bullet-}$ radical anions in Sample 1. The absorption spectrum of $S_3^{\bullet-}$ radical anions is characterized by a plateau at about 1.77 eV. However, the shape of the absorption spectrum of Sample 1 differs from the characteristic absorption of $S_3^{\bullet-}$ of lazurite [4,5]. Thus, the absorption band at 2.05 eV is not related to $S_3^{\bullet-}$ radical anions. On the other hand, in a number of works [40,41,52,53] it is noted that absorption bands at 2.05 and 2.38 eV, as well as a much less intense band about 1.33 eV, can be attributed to the absorption of *trans-* and *cis-*conformers of the neutral S_4 molecule. The authors of [40] calculated the oscillator strengths *f* for these conformals, which are equal to 0.07 and 0.047, respectively.

The observed intense ESR signal with a *g*-factor of 2.002 can be attributed to the presence of some amount of $O^{\bullet-}$ radical anions (Figure 5). Previously, blue sodalite, in which a similar ESR signal and absorption spectrum were observed, was studied in [54,55], but the nature of the color of the mineral was not fully elucidated in this work.

When this sample is heated above a temperature of 500 °C, the studied sodalite loses its color. Along with this, an absorption band appears at 3.1 eV (400 nm) upon excitation, in which intense luminescence is observed with a maximum at 1.9 eV (650 nm). Such luminescence is characteristic of $S_2^{\bullet-}$ radical anions [4].

### 3.2. Crystal Chemistry, Isomorphism, and Thermal Conversions of Haüyne

The IR spectra of initial and heated haüyne (Samples 2 and 5) are given in Figures 6–8. The spectra of initial samples contain bands of O–H stretching and bending vibrations of H_2O molecules (in the ranges of 3300–3700 and 1640–1670 cm^{-1}, respectively), antisymmetric vibrations of the CO_2 molecules (at 2341 cm^{-1}), asymmetric stretching [$F_2(\nu_3)$ mode 1135–1137 cm^{-1}] and bending [$F_2(\nu_4)$ mode, 616 cm^{-1}] vibrations of the SO_4 tetrahedra, as well as stretching (1002–1004 cm^{-1}), O–(Si,Al)–O (650–730 cm^{-1}), and Si–O–Al (in the range of 390–450 cm^{-1}) modes of the aluminosilicate framework.
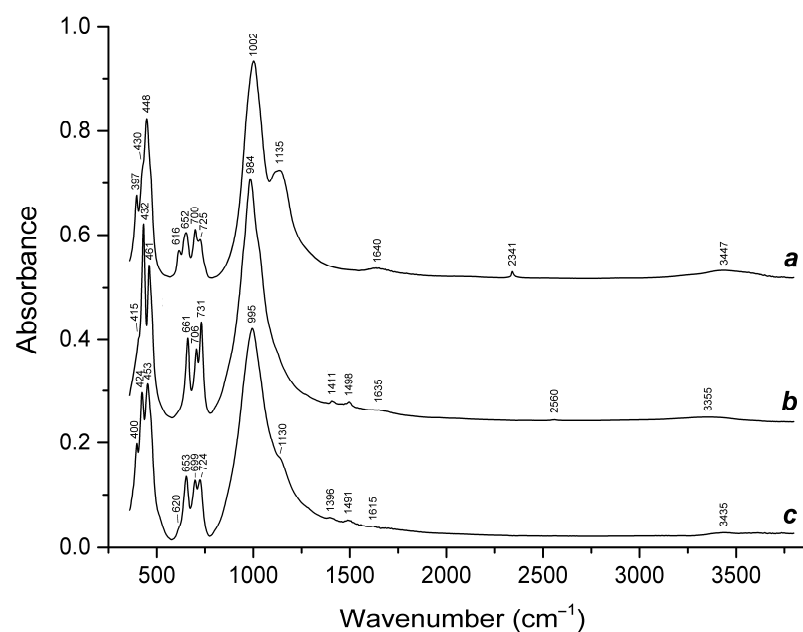
Figure 6. Infrared spectra of (**a**) initial haüyne (Sample 2), (**b**) Sample 2 preheated for three days at 700 °C, over the Fe-FeS buffer, and (**c**) preheated Sample 2 additionally annealed at 800 °C in air for one day.
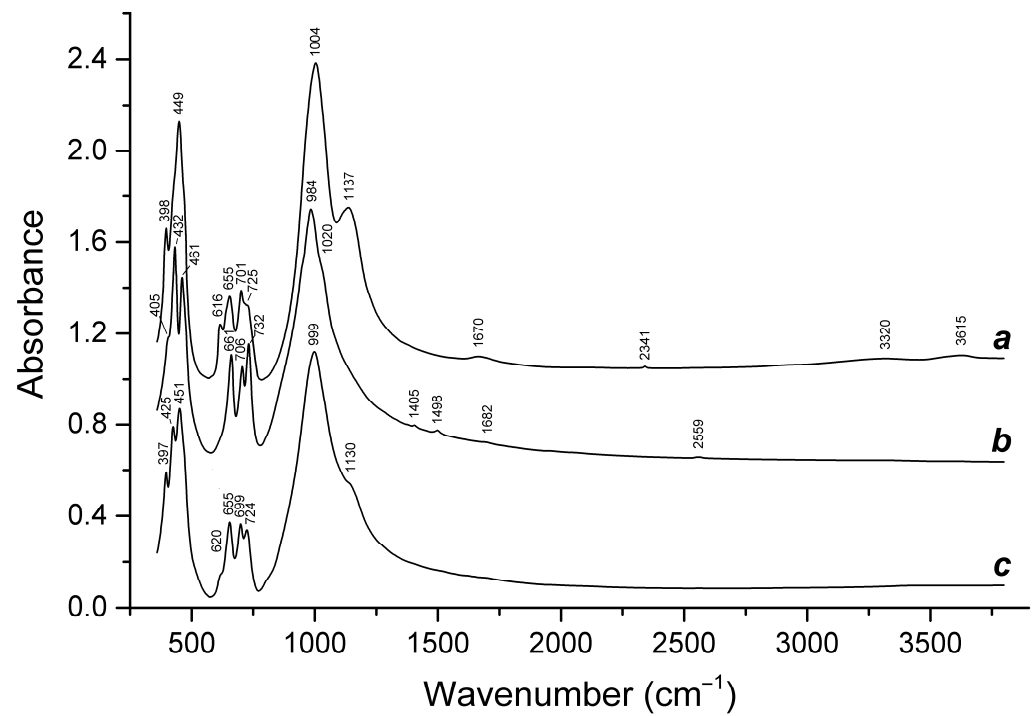
Figure 7. Infrared spectra of (**a**) initial haüyne (Sample 5), (**b**) Sample 5 preheated for three days at 700 °C over the Fe-FeS buffer, and (**c**) preheated Sample 5 additionally annealed at 800 °C in air for one day.
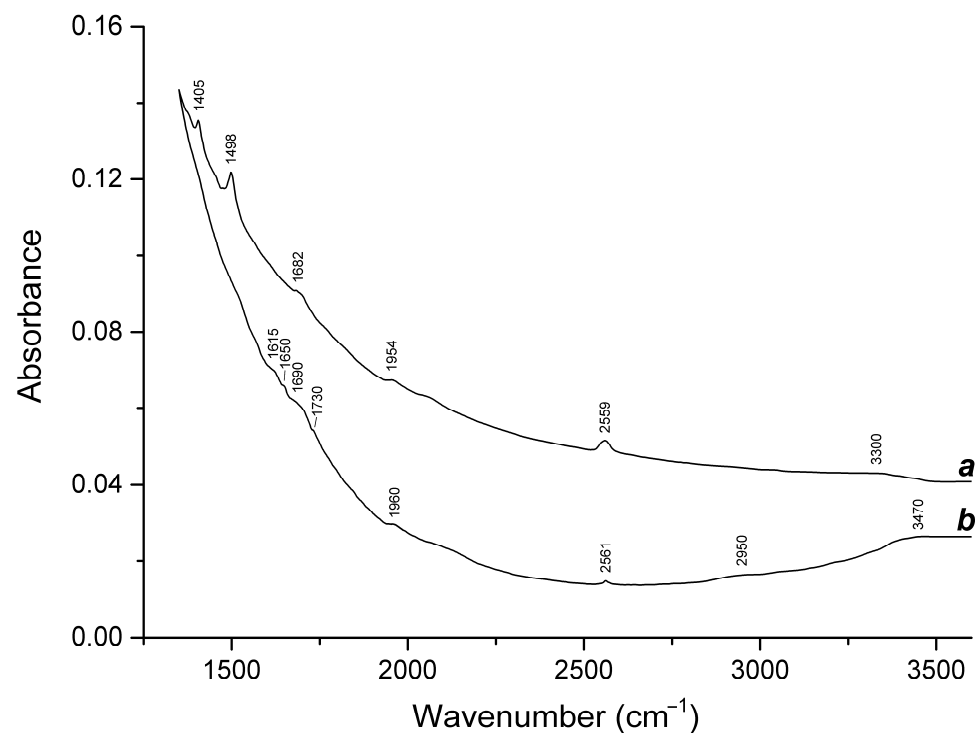
Figure 8. Infrared spectra in the 1350–3600 region of (**a**) haüyne (Sample 5) preheated for three days at 700 °C over the Fe-FeS buffer, and (**b**) preheated Sample 5 additionally annealed at 800 °C in air for one day.

Heating results in the lowering of intensities of the bands of H_2O and disappearance of the bands of SO_4^{2-} and CO_2. The samples preheated under reducing conditions change color from blue to yellow. Their IR spectra contain a weak band at 2559–2560 cm^{-1},

which is due to stretching vibrations of the HS^- anion [39]. The weak bands at 1405–1411 and 1498 cm^{-1} in the IR spectra of the preheated samples correspond to asymmetric stretching vibrations of carbonate groups required for the charge compensation. The weak band at 1954 cm^{-1} (curve *a* in Figure 8) is an overtone of stretching vibrations of the aluminosilicate framework.

It is worth noting that bands of the isolated S^{2-} anion are absent in the middle IR range, but the transformation of SO_4^{2-} into S^{2-} as a result of annealing of lazurite at 800 °C was reported [56,57]. Thus, the main scheme of transformations in the first step includes reduction of sulfate anions, and formation of S^{2-} and HS^-.

Splittings and shifts of IR bands in the preheated samples are mainly due to transformations of the framework. However, the band at 461 cm^{-1} may be partly due to vibrations of the *trans*-S_4 molecule (C_{2h} conformation) [40].

Annealing of the preheated haüyne samples at 800 °C in air results in the change of color from yellow to blue, disappearance or weakening of the band of HS^- and in the case of Sample 5, disappearance of the bands of CO_3^{2-} (Figures 1–3).

As noted above, unlike IR spectra, Raman spectra are sensitive to anionic groups and neutral molecules containing sulfide sulfur. The Raman spectra of Samples 2 and 5 are given in Figures 9 and 10.
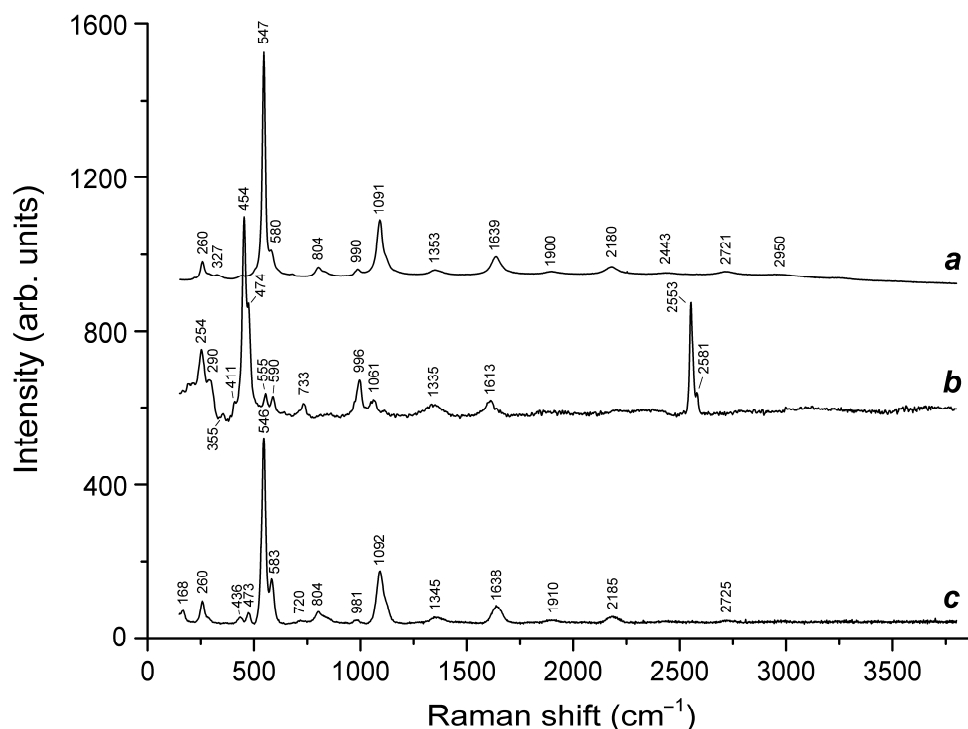
Figure 9. Raman spectra of (**a**) initial Sample 2, (**b**) Sample 2 preheated for three days at 700 °C, over the Fe-FeS buffer, and (**c**) preheated Sample 2 additionally annealed at 800 °C in air for one day.

The assignment of bands in the Raman spectra of Samples 2 and 5 and products of their thermal conversions made is given in Tables 3 and 4. The Raman spectra confirm the presence of HS^- and CO_3^{2-} anions in the products of the heating of both samples at 700 °C, over the Fe-FeS buffer. Additionally, the Raman spectra indicate the formation of oxalate $C_2O_4^{2-}$ and monosulfide S^{2-} anions, $S_2^{\bullet-}$ and $S_4^{\bullet-}$ radical anions, and S_4 molecules in the preheated samples. The Raman spectra of both initial haüyne samples and products of their annealing at 800 °C in air contain sets of characteristic bands of $S_3^{\bullet-}$ radical anions.
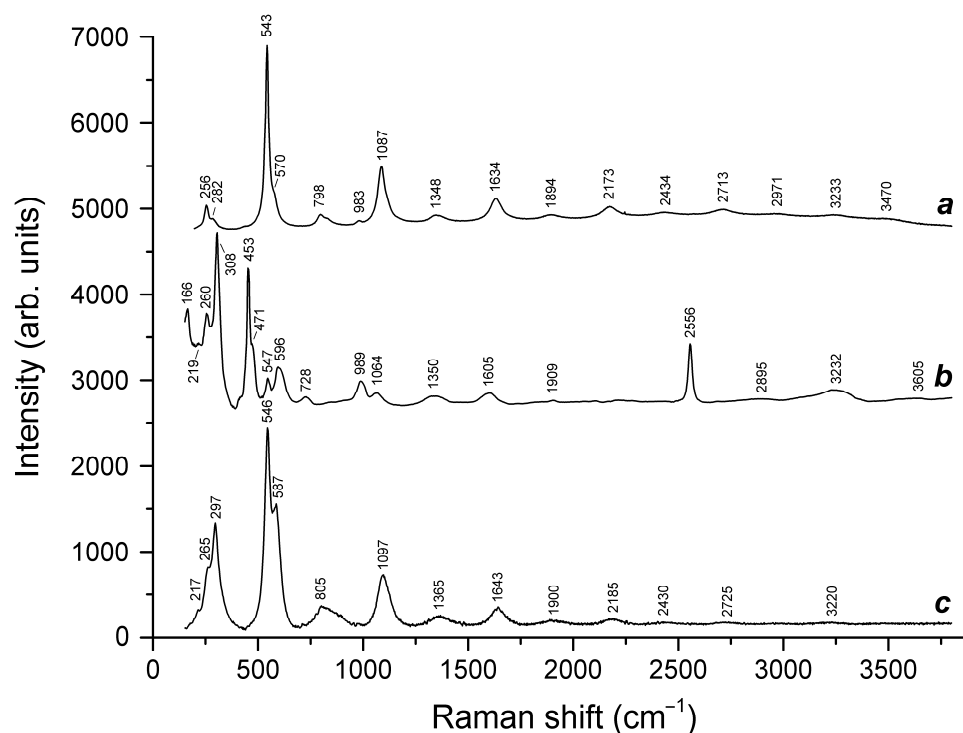
Figure 10. Raman spectra of (**a**) initial haüyne (Sample 5), (**b**) Sample 5 preheated for three days at 700 °C, over the Fe-FeS buffer, and (**c**) preheated Sample 5 additionally annealed at 800 °C in air for one day.

Table 3. Assignment of Raman bands of Sample 2 and products of its thermal conversions.

Raman Shift (cm^{-1})			Assignment
Initial Sample	Preheated Sample	Sample Heated at 800 °C in Air	
-	194w	168w	Combination of low-frequency lattice modes
-	213w	219	*trans*-S_4 bending mode
-	254	-	Bending vibrations of the $[(HS)^- Na_4]^{3+}$ cluster
260	-	260	$S_3^{\bullet-}$ bending mode (ν_2)
287w	290	-	Low–frequency lattice modes involving Na$^+$ cations and/or $S_4^{\bullet-}$ bending vibrations
-	-	-	*cis*-S_4 mixed ν_4 mode (combined symmetric bending + stretching vibrations)
327w	355w	-	*cis*-$S_4^{\bullet-}$ mixed ν_3 mode
-	-	380	*cis*-S_4 mixed ν_3 mode
448w	-	-	SO_4^{2-} [$E(\nu_2)$ mode] and/or δ[O–Si(Al)–O] bending vibrations
-	454s	-	Stretching vibrations of the $[(HS)^- Na_4]^{3+}$ cluster
-	474	473	S_6 stretching mode and/or mixed ν_4 mode of *trans*–S_4
547s	-	546s	$S_3^{\bullet-}$ symmetric stretching (ν_1) mode
	555	-	S_3 neutral molecule and/or *gauche*-S_4

Table 3. *Cont.*

Raman Shift (cm^{-1})			Assignment
Initial Sample	Preheated Sample	Sample Heated at 800 °C in Air	
580	-	583	$S_3^{\bullet-}$ antisymmetric stretching (ν_3), possibly, overlapping with the stretching band of $S_2^{\bullet-}$
-	590	-	Stretching vibrations of the $[(S^{2-})Na_4]^{2+}$ cluster and/or $S_2^{\bullet-}$ stretching mode
-	733	-	O–C–O bending vibrations of oxalate anions
-	-	720	Mixed vibrations of the aluminosilicate framework
804	-	804	$S_3^{\bullet-}$ combination mode ($\nu_1 + \nu_2$)
-	845w	-	C–C stretching vibrations of oxalate anions
990	996	981w	SO_4^{2-} symmetric stretching vibrations [$A_1(\nu_1)$ mode] and/or framework stretching vibrations
-	1061	-	CO_3^{2-} symmetric stretching vibrations
1091s	-	1092s	$S_3^{\bullet-}$ overtone ($2 \times \nu_1$)
-	1335	-	Symmetric C–O stretching vibrations of oxalate anions
1353	-	1345	$S_3^{\bullet-}$ combination mode ($2\nu_1 + \nu_2$)
-	1613	-	Antisymmetric C–O stretching vibrations of oxalate anions
1639	-	1638	$S_3^{\bullet-}$ overtone ($3 \times \nu_1$)
1900w	-	1910w	$S_3^{\bullet-}$ combination mode ($3 \times \nu_2 + \nu_1$)
2180	-	2185	$S_3^{\bullet-}$ overtone ($4 \times \nu_1$)
2443w	-	-	$S_3^{\bullet-}$ combination mode ($4 \times \nu_2 + \nu_1$)
-	2553s	-	HS^- stretching mode
-	2581w	-	H_2S symmetric stretching mode
2721	-	2725	$S_3^{\bullet-}$ overtone ($5 \times \nu_1$)
2950w	-	-	$S_3^{\bullet-}$ combination mode ($5 \times \nu_1 + \nu_2$)

Note: w—weak band, s—strong band.

Table 4. Assignment of Raman bands of Sample 5 and products of its thermal conversions.

| Raman Shift (cm^{-1})			Assignment
Initial Sample	Preheated Sample	Sample Heated at 800 °C in Air	
-	166	-	Combination of low-frequency lattice modes
-	219w	217w	*trans*-S_4 bending mode
-	260	-	Bending vibrations of the $[(HS)^-Na_4]^{3+}$ cluster
256	-	265	$S_3^{\bullet-}$ bending mode (ν_2)
282w	-	-	Low–frequency lattice modes involving Na^+ cations and/or $S_4^{\bullet-}$ bending vibrations
-	308s	297s	$S_4^{\bullet-}$ bending vibrations and/or *cis*-S_4 mixed ν_4 mode (combined symmetric bending + stretching vibrations)
-	453s	-	Stretching vibrations of the $[(HS)^-Na_4]^{3+}$ cluster

Table 4. *Cont.*

Raman Shift (cm^{-1})			Assignment
Initial Sample	Preheated Sample	Sample Heated at 800 °C in Air	
-	471	-	S_6 stretching mode and/or mixed ν_4 mode of *trans*–S_4
543s	547	546s	$S_3^{\bullet-}$ symmetric stretching (ν_1) mode
570	-	587	$S_3^{\bullet-}$ antisymmetric stretching (ν_3), possibly, overlapping with the stretching band of $S_2^{\bullet-}$
-	596	-	Stretching vibrations of the $[(S^{2-})Na_4]^{2+}$ cluster and/or $S_2^{\bullet-}$ stretching mode
-	728	-	O–C–O bending vibrations of oxalate anions
798	-	805	$S_3^{\bullet-}$ combination mode ($\nu_1 + \nu_2$)
-	850w	-	C–C stretching vibrations of oxalate anions
983w	989	-	SO_4^{2-} symmetric stretching vibrations $[A_1(\nu_1)$ mode] and/or framework stretching vibrations
-	1064	-	CO_3^{2-} symmetric stretching vibrations
1087s	-	1097s	$S_3^{\bullet-}$ overtone ($2 \times \nu_1$)
-	1350	-	Symmetric C–O stretching vibrations of oxalate anions
1348	-	1365	$S_3^{\bullet-}$ combination mode ($2\nu_1 + \nu_2$)
-	1605	-	Antisymmetric C–O stretching vibrations of oxalate anions
1634	-	1643	$S_3^{\bullet-}$ overtone ($3 \times \nu_1$)
1894w	-	1900w	$S_3^{\bullet-}$ combination mode ($3 \times \nu_2 + \nu_1$)
-	1909w	-	Overtone of SO_4^{2-} symmetric stretching vibrations?
2173	-	2185	$S_3^{\bullet-}$ overtone ($4 \times \nu_1$)
2434w	-	2430w	$S_3^{\bullet-}$ combination mode ($4 \times \nu_2 + \nu_1$)
-	2556s	-	HS$^-$ stretching mode
2713	-	2725	$S_3^{\bullet-}$ overtone ($5 \times \nu_1$)
2971w	-	-	$S_3^{\bullet-}$ combination mode ($5 \times \nu_1 + \nu_2$)
3233w, 3470w	3232, 3605w	3220w	O–H stretching modes

In the original Sample 3, no $S_3^{\bullet-}$ centers were observed before heating. Two absorption bands with maxima at 525 and 585 nm are associated with $S_4^{\bullet-}$ centers in different configurations, and a weak absorption band at 400 nm corresponds to $S_2^{\bullet-}$ centers (Figure 11) [4,58]. Being excited in the 400 nm region, the samples show intense luminescence with a maximum in the 650 nm region associated with these $S_2^{\bullet-}$ radical anions.

In the ESR spectrum, in addition to six lines associated with Mn^{2+} centers in calcite inclusions, there is a signal with *g*-tensor components of 2.034 and 2.021, associated with $S_4^{\bullet-}$ centers (Figure 12) [58]. As a result of heating the sample, the intensity of this signal decreases, together with a weakening of the absorption bands. At temperatures above 400 °C, the $S_4^{\bullet-}$—centers disappear.
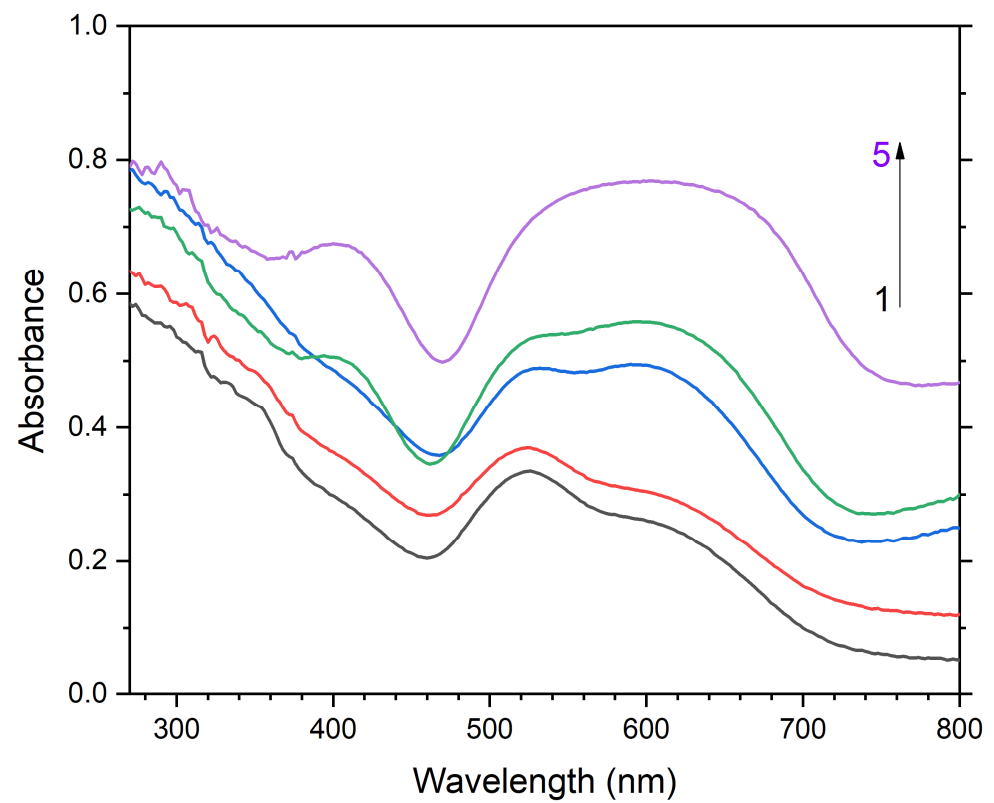
Figure 11. Spectra of diffuse absorption of haüyne (Sample 3): unheated sample (1) and samples heated at 200 °C (2), 400 °C (3), 600 °C (4), and 800 °C (5).
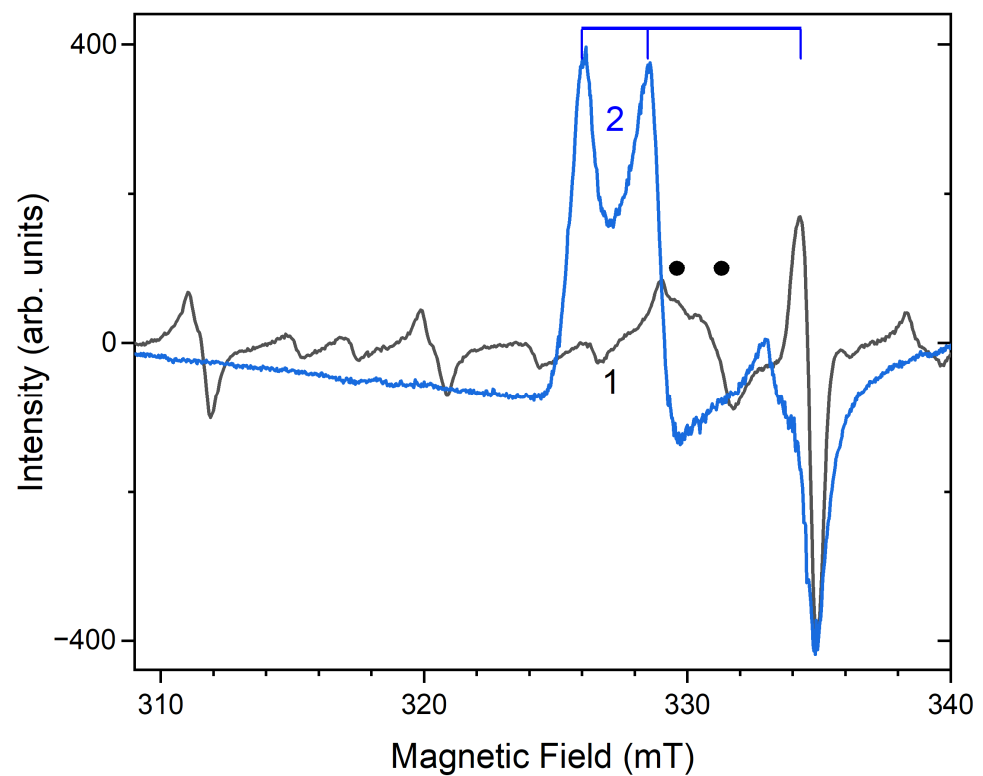
Figure 12. The ESR spectra of unheated haüyne (Sample 3) (1) and Sample 3 heated at a temperature of 800 °C (2). The dots indicate the bands of $S_4^{\bullet-}$ and the vertical lines show the bands of $S_3^{\bullet-}$.

The intensities of the absorption band and luminescence associated with $S_2^{\bullet-}$ centers increase in this case. At temperatures above 700 °C, a signal with $g_1 = 2.056$, $g_2 = 2.041$, and $g_3 = 2.008$, associated with $S_3^{\bullet-}$ centers, appears in the ESR spectrum. At the same time, the shape of the absorption band in the region of 600 nm changes, it acquires a table-like shape, and its intensity also begins to grow. The sample acquires an intense blue color, also associated with the $S_3^{\bullet-}$ radical anion [4]. In this case, the absorption band in the region of 400 nm and the luminescence associated with the $S_2^{\bullet-}$ centers begin to decrease. The temperature dependences of the observed effects are shown in Figure 13.
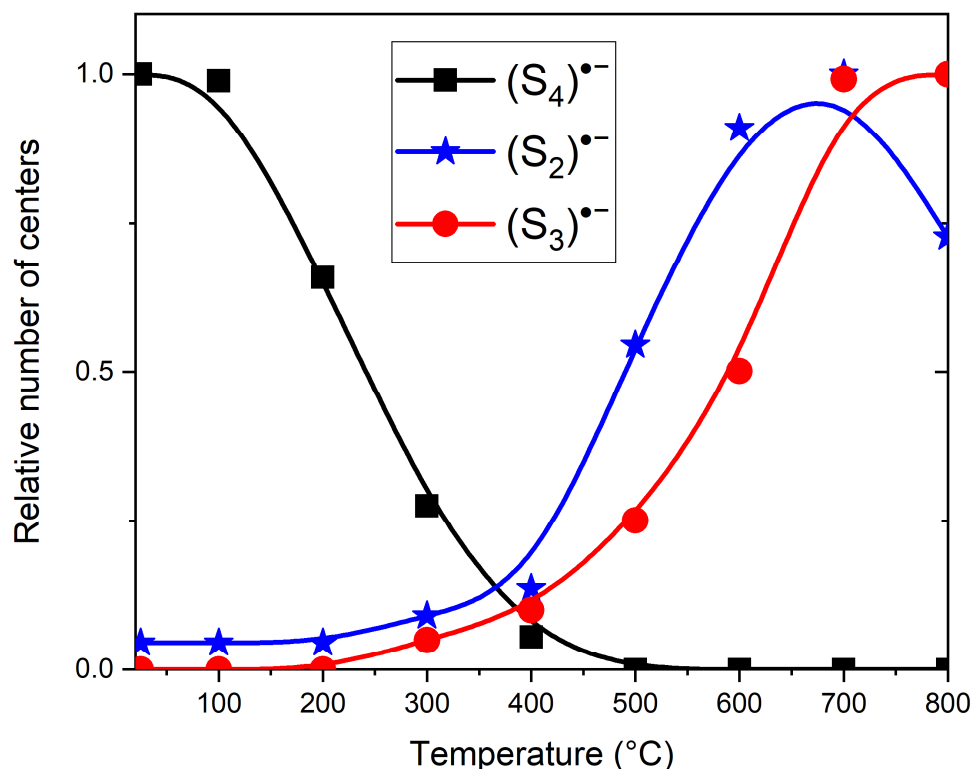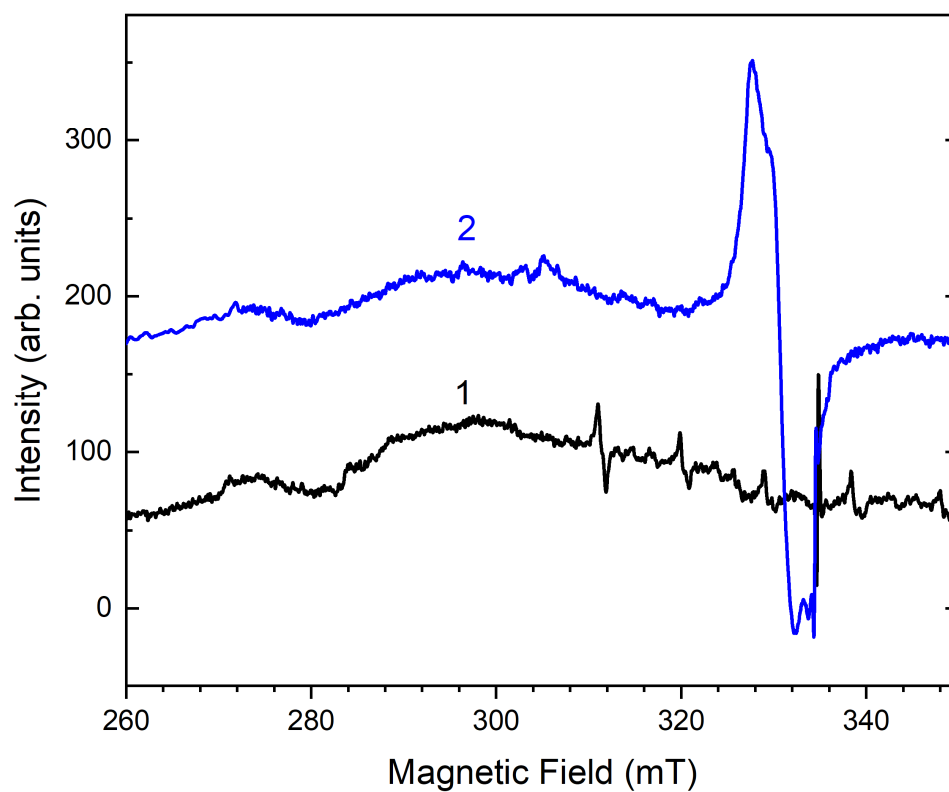

Figure 13. Relative amounts of various sulfur radical anions in haüyne (Sample 3) heated at different temperatures. The values of the relative amounts are normalized to the maximum number of each of the radical anions.

The absorption spectrum of initial sample 4 shows a broad band at 600 nm, which is also associated with $S_3^{\bullet-}$ radical anions, as well as a sharp rise in the region of 280 nm, which can be caused by the absorption of $S_6^{\bullet-}$ radical anions (Figure 14) [39,58,59]. In the original sample 4, a weak signal with the *g*-tensor components $g_1 = 2.045$, $g_2 = 2.034$, and $g_3 = 2.008$, associated with $S_3^{\bullet-}$ radical anions [4], as well as a signal with the *g*-tensor components $g_1 = 2.011$ and $g_2 = 2.006$, associated with the radical anion $S_6^{\bullet-}$ [45,58,60], are observed (Figure 15).

When the sample was heated above 500 °C, the ESR signal with $g_1 = 2.011$ and $g_2 = 2.017$ decreases together with a decrease in the rise intensity in the region of 280 nm. Along with this, the sample acquires a saturated blue color, which is accompanied by an increase in the ESR signal with $g_1 = 2.045$, $g_2 = 2.034$, and $g_3 = 2.008$, as well as absorption bands in the region of 600 nm associated with $S_3^{\bullet-}$ radical anions. The temperature dependences built on the basis of the analysis of the absorption and EPR spectra are shown in Figure 16.
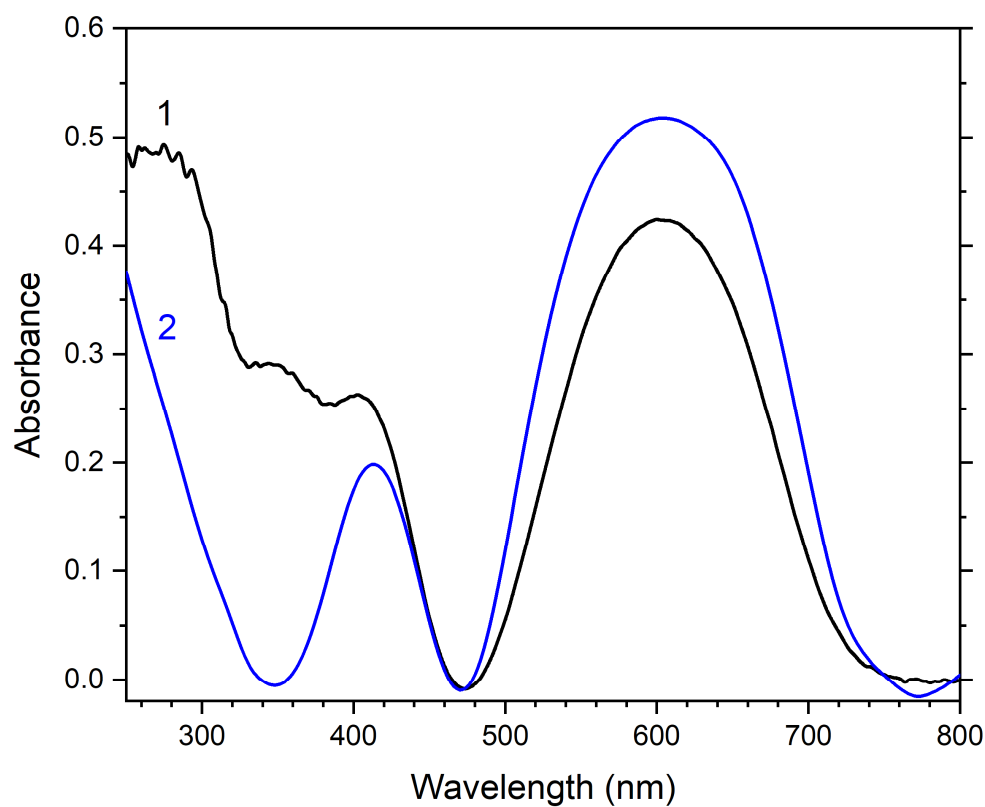
Figure 14. Diffuse absorption spectra of original haüyne (Sample 4) (1) and Sample 4 heated at 800 °C (2).

Figure 15. The ESR spectra of original haüyne (Sample 4) (1) and Sample 4 heated at 800 °C (2). The black triangles show the bands of the $S_6^{\bullet-}$ radical anions bands, and the vertical blue lines indicate the bands of $S_3^{\bullet-}$.
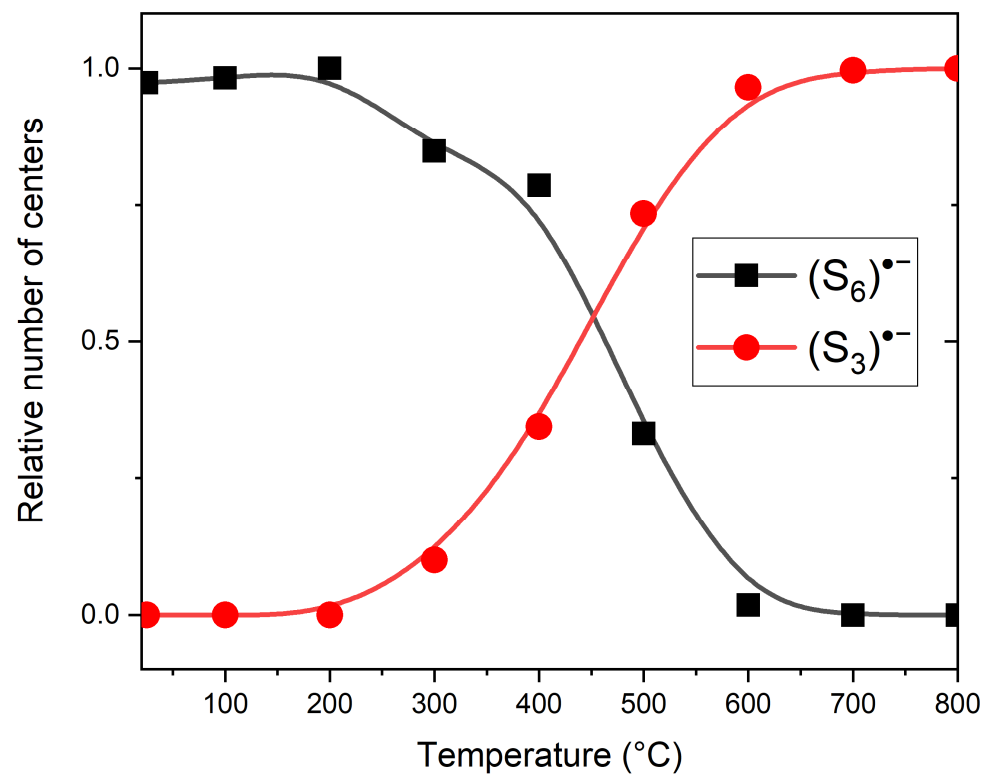
Figure 16. Relative amounts of polysulfide radical anions in haüyne (Sample 3) heated at different temperatures. The values of the relative amounts are normalized to the maximum number of each of the radical anions.

The blue color of Sample 2 is due to the presence of the $S_3^{\bullet-}$ radical anions, which are easily identified by an ESR signal with g_1 = 2.049, g_2 = 2.035, and g_3 = 2.010 (Figure 17, curve 1). After heating in reducing atmosphere using the Fe/FeS buffer at 700 °C, the color of the sample changes to yellow, and the ESR signal associated with the $S_3^{\bullet-}$ radical anion disappears (Figure 17, curve 2). During subsequent heating at 800 °C, the blue color is partially restored and an ESR signal with g_1 = 2.049, g_2 = 2.035, and g_3 = 2.010 appears (Figure 17, curve 3). However, its intensity is less than that of the original sample.

The observed results show that various polysulfide radical anions are converted into $S_2^{\bullet-}$ and $S_4^{\bullet-}$ radical anions and S_4 neutral molecules during heating at 700 °C in a reducing atmosphere, whereas the $S_3^{\bullet-}$ radical anion is stable during heating at 800 °C in air. These data do not contradict the experimental results obtained in [61,62], where it was shown that various sulfur radicals are converted into $S_2^{\bullet-}$ and $S_3^{\bullet-}$ radical anions when heated.

It should be noted that the values of the g-tensor components of the $S_3^{\bullet-}$ radical anions formed during heating of most S-bearing sodalite-group minerals studied in this work and elsewhere [58] are close to those of the g tensor of $S_3^{\bullet-}$ in haüyne and some synthetic sodalites [4,63]. The only exception is $S_3^{\bullet-}$ radical anion in Sample 3 heated in air: its values of the g-tensor components are close to those of $S_3^{\bullet-}$ or $S_3^{\bullet-}$ occurring in minerals of the cancrinite group [58,63].

Annealing of preheated powdered Sample 5 at 800 °C in air results in gradual enhancement of its unit cell parameter from 8.04 to 8.97 Å, accompanied by its transformation into a new cubic phase with the a parameter growing from 9.05 to 9.08 Å during 32 h (Figure 18). This transformation is accompanied by broadening and shifts of reflections.
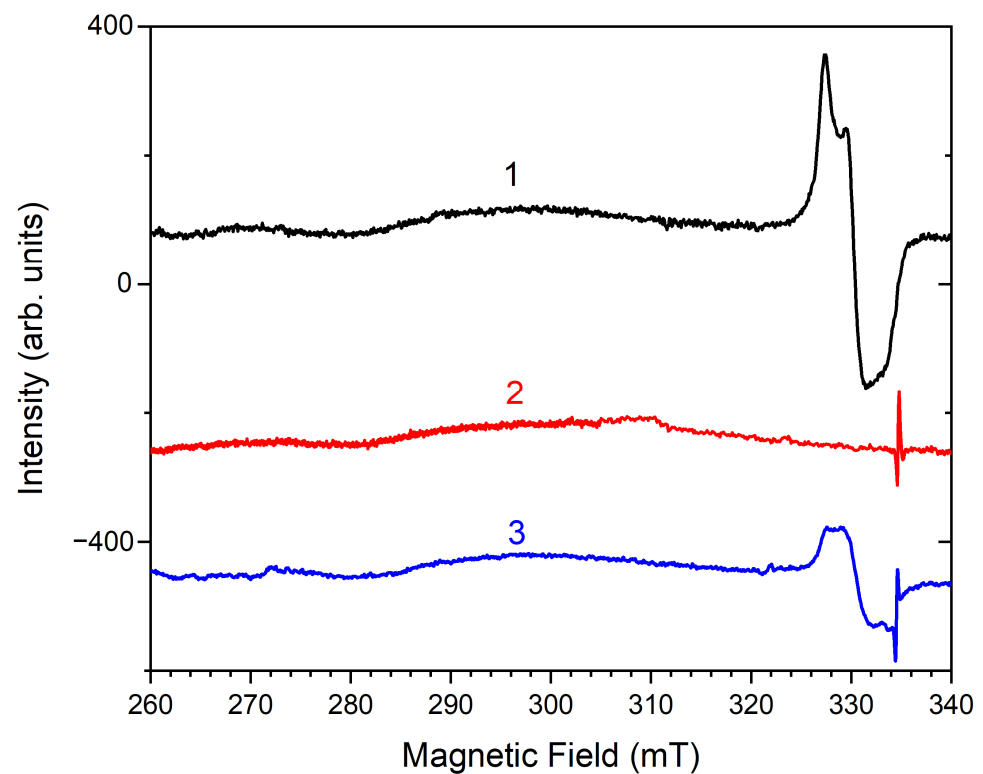
Figure 17. ESR spectra of initial haüyne (Sample 2) (1), and Sample 2 heated at 700 °C under buffer (2) and at 800 °C in air (3).
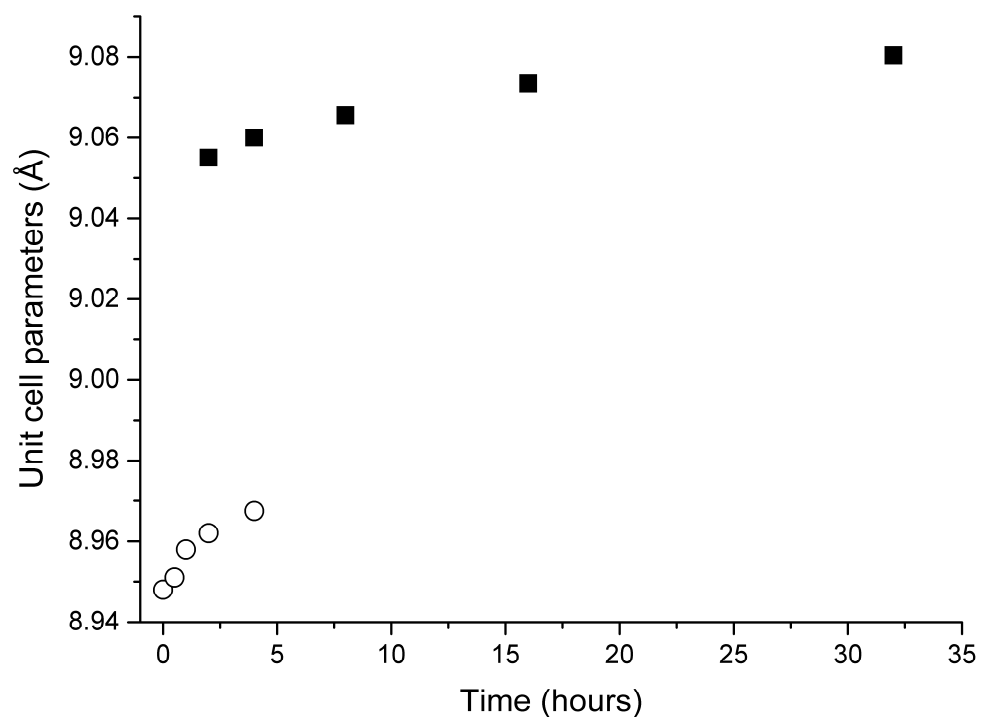
Figure 18. Kinetics of changes of the cubic unit cell parameter of the initial phase of the preheated haüyne (Sample 5, circles) and product of its annealing at 800 °C (squares).

The initial phase with a smaller *a* parameter disappears five hours after the start of annealing. The final product of annealing is pale blue. Annealing of preheated single-crystal grains of Sample 5 at 800 °C during 32 h results in the formation of a greenish blue cubic phase. Based on the above spectroscopic data, one can conclude that the enhancement

of the unit cell parameter during annealing is caused by the transformation of small extra-framework anions (S^{2-} and HS^-) into larger ones (SO_4^{2-} and, to a lesser extent, $S_3^{\bullet-}$). Thus, the process observed during annealing has the character of a phase transition, and both in the initial and in the final phase, the degree of sulfur oxidation (and, consequently, the unit cell parameter) can vary smoothly within relatively narrow limits.

The observed abrupt increase in the unit cell parameter may indicate that the formation of the new phase proceeds by the nucleation mechanism. Partial oxidation of sulfur in the preheated sample at the initial stage of calcination leads to a broadening of the lines in the diffraction patterns, which may indicate the inhomogeneity of the composition and associated mechanical stresses in the crystal.

3.3. Thermal Conversions of Slyudyankaite

Slyudyankaite, ideally $Na_{28}Ca_4(Si_{24}Al_{24}O_{96})(SO_4)_6(S_6)_{1/3}(CO_2)\cdot 2H_2O$, is a triclinic sodalite-group mineral containing sodalite cages of two kinds. Cages of the first type contain Na^+ and Ca^{2+} cations and SO_4^{2-} anions as well as trace amounts of $S_3^{\bullet-}$ radical anions. Cages of the second type contain only neutral molecules (cyclic S_6 having chair-like conformation, CO_2, H_2O, and subordinate S_4).

The IR spectrum of slyudyankaite (curve *a* in Figure 19) contains bands of O–H stretching vibrations of hydrogen bonds of medium strength (3380 to 3610 cm^{-1}), strong hydrogen bond or strong dipole-dipole interactions with CO_2 molecules (shoulder at 3240 cm^{-1}), antisymmetric stretching vibrations of free $^{12}CO_2$ molecules and $^{12}CO_2$ molecules which are acceptors of strong hydrogen bonds (2341 and 2385 cm^{-1}, respectively), antisymmetric stretching vibrations of the $^{13}CO_2$ molecules (2275 cm^{-1}), C–O stretching vibrations of trace admixture of O=C=S molecules (a very weak band at 2040 cm^{-1}), bending vibrations of H_2O molecules (at 1632 cm^{-1} with an indistinct shoulder at ~1680 cm^{-1} which may correspond to H_2O molecules forming strong hydrogen bonds), asymmetric stretching vibrations of the SO_4^{2-} anionic groups [the degenerate $F_2(\nu_3)$ mode] (1138 and 1107 cm^{-1}), stretching vibrations of the aluminosilicate framework (1002 cm^{-1}), mixed vibrations of the aluminosilicate framework (in the range of 650–720 cm^{-1}), stretching vibrations of the neutral S_4 molecule having *cis* conformation (641 cm^{-1}), bending vibrations of the SO_4^{2-} anionic groups [the degenerate $F_2(\nu_4)$ mode] (614 cm^{-1}), and lattice modes involving bending vibrations of the aluminosilicate framework and librations of SO_4^{2-} and extra-framework molecules (below 550 cm^{-1}). An indistinct shoulder at ~465 cm^{-1} may be partly due to stretching vibrations of the cyclic S_6 molecule having D_{3d} symmetry [41].

Changes in the IR spectrum of slyudyankaite that occur as a result of its calcination are basically similar to those observed during calcination of the haüyne samples described above: the bands of O–H stretching vibrations, CO_2, S_4, and S_6 molecules, and SO_4^{2-} anions disappear or become weaker. In the IR spectrum of Sample 6 preheated at 700 °C under reducing conditions, a weak band of HS^- is observed at 2561 cm^{-1}. Both heated samples (preheated and annealed at 800 °C in air) contain bands of CO_3^{2-} anions in the range of 1390–1500 cm^{-1}. Unlike IR spectra of heated haüyne (Samples 2 and 5), spectral curves of both preheated and annealed at 800 °C, slyudyankaite samples have a weak shoulder at 1275 cm^{-1}, which may correspond to the BO_3^{3-} anion. If this assumption is correct, then it follows that initial slyudyankaite contained boron in the four-fold coordination, which could not be detected by means of IR spectroscopy because IR bands of the BO_4 tetrahedron overlap with bands of the aluminosilicate framework.

Raman spectra of slyudyankaite and products of its heating are presented in Figure 20. The assignment of Raman bands is given in Table 5.
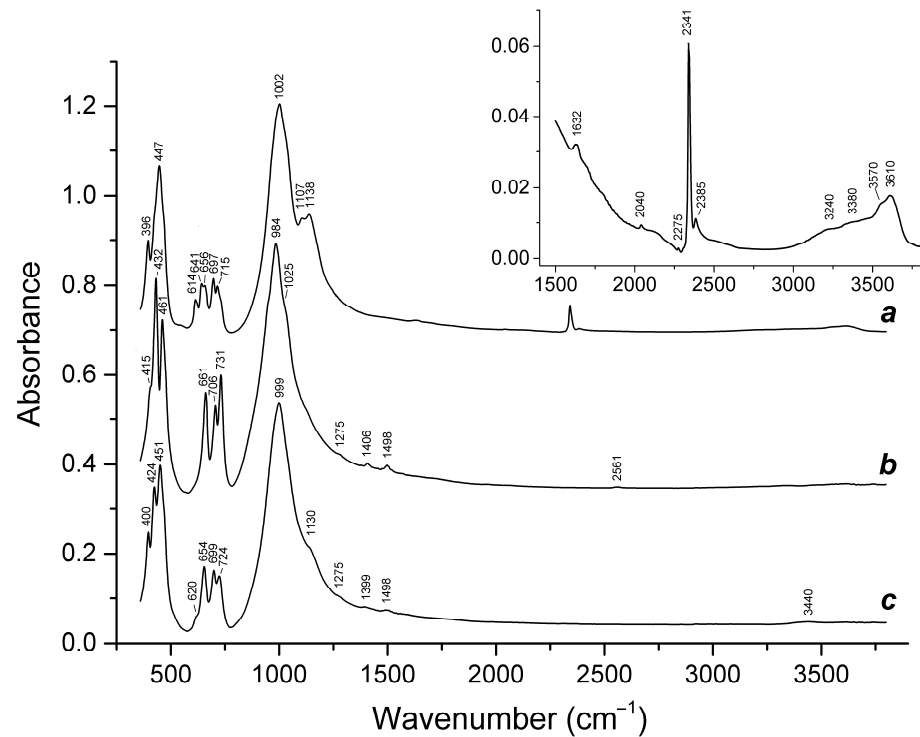
Figure 19. Infrared spectra of (**a**) initial slyudyankaite (Sample 6), (**b**) Sample 6 preheated for three days at 700 °C, over the Fe-FeS buffer, and (**c**) preheated Sample 6 additionally annealed at 800 °C in air for one day. The inset shows the IR spectrum of initial Sample 6 in the range of 1500–3800 cm^{-1}.
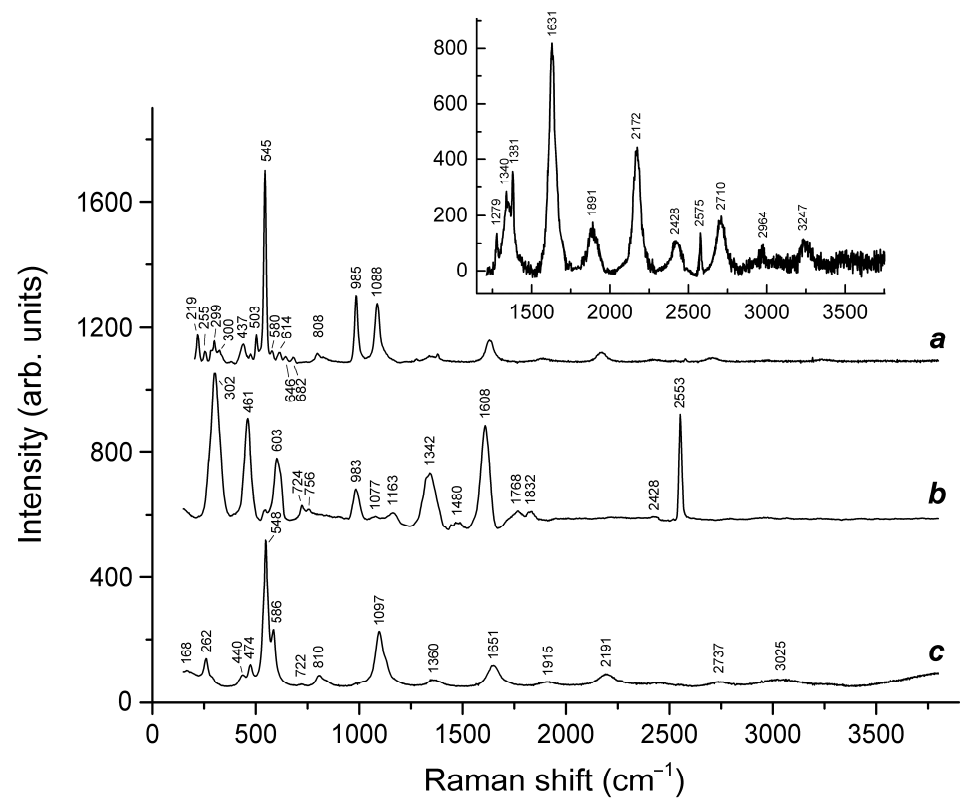
Figure 20. Raman spectra of (**a**) initial slyudyankaite (Sample 6), (**b**) Sample 6 preheated for three days at 700 °C, over the Fe-FeS buffer, and (**c**) preheated Sample 6 additionally annealed at 800 °C in air for one day. The inset shows the Raman spectrum of initial Sample 6 in the range of 1200–3750 cm^{-1}.

Table 5. Assignment of Raman bands of slyudyankaite and products of its thermal conversions.

Raman Shift (cm^{-1})			Assignment
Initial Sample	Preheated Sample	Sample Heated at 800 °C in Air	
219	-	-	*trans*-S_4 bending
260	-	262	$S_3^{\bullet-}$ bending A_2 (ν_2) and S_6 (with D_{3d} symmetry) bending
283	-	-	Framework bending vibrations (resonance with a S_6 bending mode?)
298	302s	-	$S_4^{\bullet-}$ bending vibrations
330	-	-	*cis*-S_4 mixed ν_4 mode (symmetric bending + stretching)
380w	-	-	*cis*-S_4 mixed ν_3 mode
437	-	440w	SO_4 [bending E (ν_2) mode] and/or S_6 (mixed mode)
-	461s	-	[(HS)Na$_4$]$^{3+}$ stretching vibrations
477	-	474	S_6 stretching mode and/or mixed ν_4 mode of *trans*-S_4
503	-	-	Bending vibrations of the framework
545s	-	548s	$S_3^{\bullet-}$ symmetric stretching (ν_1) (possibly, overlapping with the stretching band of *gauche*-S_4)
580	-	586	$S_3^{\bullet-}$ antisymmetric stretching mode (ν_3)
-	603	-	$S_2^{\bullet-}$ stretching mode
614	-	-	SO_4^{2-} [bending F_2 (ν_4) mode]
645	-	-	*cis*-S_4 stretching
682	-	-	*trans*-S_4 symmetric stretching ν_3 mode
-	724, 756w	722w	O–C–O bending vibrations of oxalate anions
807	-	810	$S_3^{\bullet-}$ combination mode ($\nu_1 + \nu_2$)
985s	983	-	SO_4^{2-} [symmetric stretching A_1 (ν_1) mode] (possibly, overlapping with the weak band of framework stretching vibrations)
-	1077w	-	CO_3^{2-} symmetric stretching mode
1088s	-	1097s	$S_3^{\bullet-}$ overtone ($2 \times \nu_1$) [possibly, overlapping with the $SO_4^{\bullet-}$ stretching band ($\nu_3 - F_2$)]
-	1163	-	$S_2^{\bullet-}$ overtone ($2 \times \nu_1$)
1279, 1381	-	-	Symmetric stretching vibrations of CO_2 molecules (Fermi doublet, resonance with the overtone of bending vibrations).
1340	1342	1360	Symmetric C–O stretching vibrations of CO_2 molecules—involved in strong dipole-dipole interactions and/or symmetric C–O stretching vibrations of acid oxalate anions
-	1480w	-	CO_3^{2-} asymmetric stretching mode
-	1609s	-	Antisymmetric C–O stretching vibrations of acid oxalate anions
1631	-	-	$S_3^{\bullet-}$ overtone ($3 \times \nu_1$)
-	-	1651	Symmetric C–O stretching vibrations of oxalate anions
-	1768, 1832	-	C=O stretching vibrations of acid oxalate groups

Table 5. *Cont.*

|	Raman Shift (cm^{-1})		Assignment
Initial Sample	Preheated Sample	Sample Heated at 800 °C in Air	
1891	-	1915	$S_3^{\bullet-}$ combination mode ($3 \times \nu_1 + \nu_2$)
2172	-	2191	$S_3^{\bullet-}$ overtone ($4 \times \nu_1$)
2428w	-	-	$S_3^{\bullet-}$ combination mode ($4 \times \nu_2 + \nu_1$)
-	2553s	-	HS^- stretching mode
2575w	-	-	H_2S symmetric stretching mode
2710	-	2737	$S_3^{\bullet-}$ overtone ($5 \times \nu_1$)
2964w	-	-	$S_3^{\bullet-}$ combination mode ($5 \times \nu_1 + \nu_2$)
3025	-	-	O–H stretching vibrations
3247w	-	-	$S_3^{\bullet-}$ overtone ($6 \times \nu_1$)

The Raman spectrum of the initial slyudyankaite sample contains bands of SO_4^{2-} anions, $S_3^{\bullet-}$ radical anions, and different neutral molecules (*cis-* and *trans*-S_4, S_6, H_2S, and CO_2). Preheating of slyudyankaite at 700 °C under reducing conditions results in the transformation of S-bearing species into HS^-, $S_2^{\bullet-}$, and $S_4^{\bullet-}$ and, possibly, monosulfide anion S^{2-}, which could not be detected by means of vibrational spectroscopy methods but is required for the charge balance. Note that S^{2-} was identified as the main extra-framework anion in the crystal structure of the product of thermal conversions of lazurite under the same conditions [57]. Reduction of CO_2 occurring in initial slyudyankaite results in the formation of carbonate and acid oxalate anions.

Further annealing of preheated slyudyankaite at 800 °C in air results in the disappearance of HS^-, $S_2^{\bullet-}$, and $S_4^{\bullet-}$, restoration of the SO_4^{2-} and $S_3^{\bullet-}$ anionic groups, and transformation of acid oxalate groups into neutral ones. Bands of $S_3^{\bullet-}$ in the Raman spectrum of the annealed slyudyankaite are shifted towards higher frequencies as compared to analogous bands of the initial sample, which may indicate their occurrence in a straitened state.

3.4. Sodalite—Sapozhnikovite Solid-Solution Series

Sodalite, ideally $Na_8(Al_6Si_6O_{24})Cl_2$, and sapozhnikovite, its hydrosulfide-dominant structural analogue with the formula of the hypothetical end-member $Na_8(Al_6Si_6O_{24})(HS)_2$ form a solid-solution (isomorphous) series in which the Cl^-:HS^- (simply, Cl:S) ratio is the only significant variable. In the studied specimens from Karnasurt Mt. (Lovozero alkaline massif), this ratio varies from $[Cl_{1.11}(HS)_{0.84}]_{\Sigma1.95}$ to $[(HS)_{1.57}Cl_{0.38}]_{\Sigma1.95}$ (Table 1; Figure 21). Samples with Cl > S (in atom proportions) belong to the mineral species sodalite, whereas samples with S > Cl belong to sapozhnikovite. Slight deficiency of the Cl + S sum in comparison with the ideal value 2.00 atoms per formula unit (Table 1; Figure 21) is caused by the presence of minor amounts of H_2O in these minerals [39], probably together with Cl^- and HS^- anions in sodalite cages. The presence of water also explains slight deficiency of analytical totals in all electron-microprobe analyses of sodalite–sapozhnikovite series minerals (Table 1).
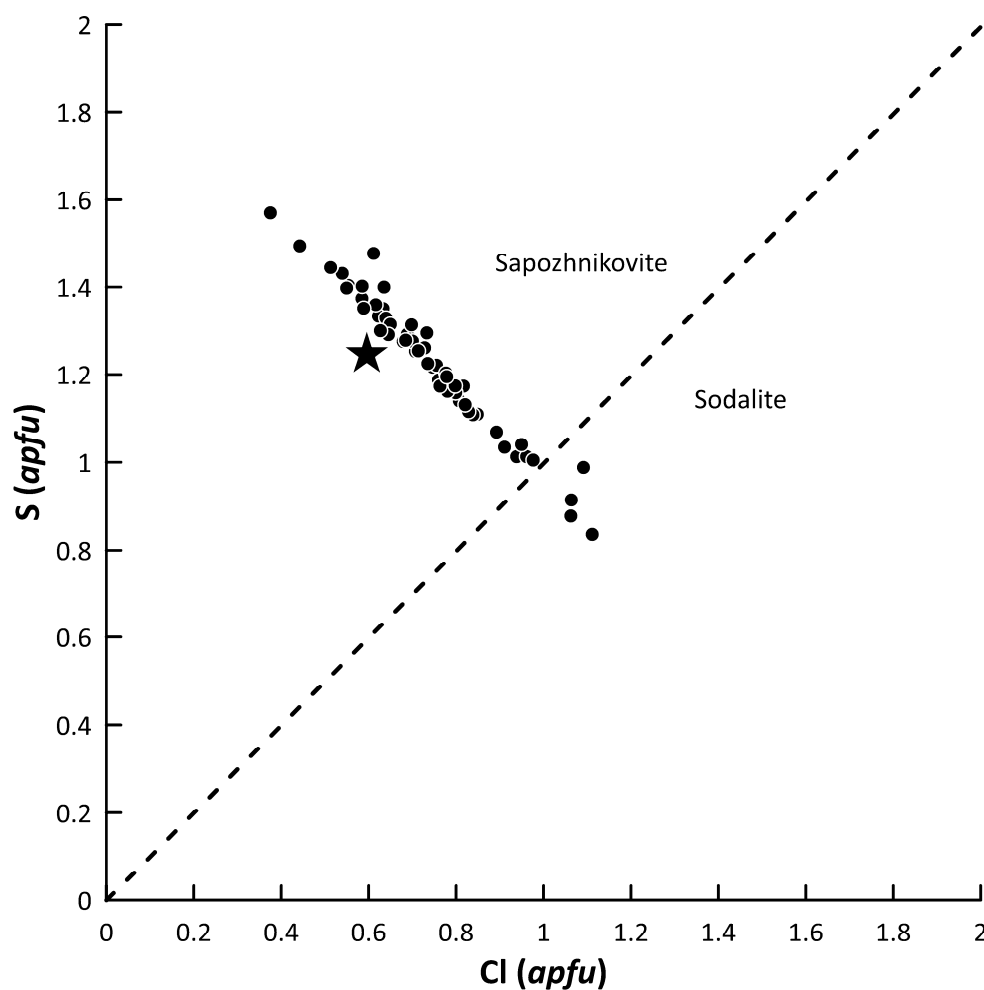
Figure 21. Variations of the contents of Cl and S atoms per formula unit (*apfu*) in minerals belonging to the sodalite–sapozhnikovite solid-solution series from Karnasurt Mt., Lovozero massif, Kola Peninsula, Russia.

In the interval $[Cl_{1.11-0.38}(HS)_{0.84-1.57}]$, this homovalent isomorphous series is continuous (Figure 21). We suggest this interval is caused by geochemical features rather crystal chemical constraints.

4. Discussion

4.1. General Remarks on the Isomorphism of Extra-Framework Components in Sodalite-Group Minerals

The general common formula of cubic alkaline aluminosilicates belonging to the sodalite group is $ABNa_6(Si_6Al_6O_{24})XY$, where the pairs of cationic and anionic extra-framework components $AB + XY$ are $Na_2 + Cl_2$ for sodalite, $Na_2+(HS)_2$ for sapozhnikovite, $K\square+F(H_2O)_4$ for bolotinaite, $Na_2+(SO_4)(H_2O)$ for nosean, $Ca_2+(SO_4)_2$ for haüyne, and $NaCa+(S_3{}^{\bullet-})(SO_4)$ for lazurite. However, the application of a complex of spectroscopic methods in this work and elsewhere [3,4,64] shows that the crystal chemistry of subordinated components in cubic sodalite-group aluminosilicates is much more complex. In particular, H^+, H_3O^+, $CO_3{}^{2-}$, OH^-, S^{2-}, $S_2{}^{\bullet-}$, S_3, *cis-* and *trans-*$S_4{}^{\bullet-}$, $SO_3{}^{\bullet 2-}$, $SO_4{}^{\bullet 2-}$, *cis-*, *trans-* and *gauche-*S_4, S_6, CO_2, COS, and HF were identified as extra-framework species in these minerals. Experiments with annealing show that these components take part in complex thermal conversions involving some additional components, e.g., oxalate anions. Similar transformations can occur in natural mineral assemblages. Thus, the composition of sodalite-group minerals may serve as a marker of mineral-forming media including fugacities of volatile components (H_2O, O_2, CO_2, HF, SO_2, and polysulfide compounds).

In general, similar processes were observed in sulfur-enriched fluids [61,62]. Apparently, when heated, the channel widths increase, which allows complex anion radicals to migrate and disproportionate with the formation of the most stable radical anion radicals ($S_3^{\bullet-}$ or $S_2^{\bullet-}$, depending on the redox conditions). Along with this, dehydration of the studied samples also occurs, which also facilitates the migration of polysulfide species.

4.2. Sapozhnikovite as a Marker of Reducing Conditions

Experiments with heating of haüyne under reducing conditions (in the presence of Fe-FeS buffer) show that the main scheme of transformations of extra-framework components is $SO_4^{2-} \rightarrow S^{2-} + 2O_2(\text{gas})$, and a subordinate process is $CO_2 + 2SO_4^{2-} + H_2O \rightarrow 2HS^- + CO_3^{2-} + 4O_2(\text{gas})$. The conversions $3SO_4^{2-} \rightarrow S_3^{\bullet-} + 5e + 6O_2(\text{gas})$, $2S_3^{\bullet-} \rightarrow S_2^{\bullet-} + S_4^{\bullet-}$, and $2CO_2 + 2e \rightarrow C_2O_4^{2-}$ (e = electron) are the additional channels of haüyne transformations during their heating at 700 °C under reducing conditions.

Thus, HS^- and $C_2O_4^{2-}$ anions are stable only under reducing conditions. Data on the occurrence of sapozhnikovite $Na_8(Al_6Si_6O_{24})(HS)_2$ confirm this conclusion. Crystallization of aegirine $NaFe^{3+}Si_2O_6$, which precedes formation of sapozhnikovite, could be accompanied by the following redox reactions: $Na_2O + 2FeO + 4SiO_2 + CO_2 \rightarrow 2NaFeSi_2O_6 + CO$; $Na_2O + 2FeO + 4SiO_2 + 0.5CO_2 \rightarrow 2NaFeSi_2O_6 + 0.5C$, where C is carbon with the oxidation degree of 0 [39]. During the crystallization of aegirine, iron occurring as Fe^{2+} in the fluid is fixed as Fe^{3+} in the solid phase. Such processes are possible only in peralkaline media with a high Na:Ca ratio (otherwise, hedenbergite $CaFe^{2+}Si_2O_6$ is formed instead of aegirine). Similar reactions, e.g., $2Na_2O + 4FeO + 4SiO_2 + 2SO_3 + 2OH^- + O_2 \rightarrow 4NaFeSi_2O_6 + 2HS^-$, could lead to the formation of reduced forms of sulfur, including HS^- anions.

The redox processes in sodalite-group minerals discussed above involve species hosted by sodalite cages as well as gaseous O_2. However, in the case of sapozhnikovite, an alternative mechanism including incorporation of HS^- as a result of the exchange reaction of sodalite with a late reduced fluid is not excluded.

Unlike CO_2 molecules, carbonate anions rarely occur in sodalite-group minerals in significant amounts. An unusual CO_3^{2-}-bearing mineral with the sodalite-type framework, empirical formula $(Na_{5.28}K_{0.40}Ca_{1.23}Fe_{0.01})(Si_{5.93}Al_{6.07}O_{24.01})(SO_4)_{0.77}Cl_{0.94}(CO_3)_{0.30}$ and unit cell parameter $a = 9.0352$ Å has been discovered in a metasomatic ejectum from Mount Vesuvio, Italy and its crystal structure has been solved [65]. Taking into account above-described thermal transformations of CO_2 in haüyne and the fact that the CO_3-bearing sodalite-group mineral from Vesuvio underwent heating during metasomatism, it is reasonable to suppose that CO_3^{2-} anions in this mineral were formed as a result of the transformation $CO_2 + 2SO_4^{2-} + H_2O \rightarrow 2HS^- + CO_3^{2-} + 4O_2(\text{gas})$ in an initial sodalite-group mineral. In the experiments with heating of haüyne under reducing conditions, CO_2 molecules occurring in sodalite cages partly transformed into neutral or acid oxalate anions. In this regard, the association of sapozhnikovite with kyanoxalite (a cancrinite-group mineral containing neutral or acid oxalate anions) is indicative.

Experiments with annealing of sulfate sodalite-group minerals show that under high-temperature oxidizing conditions (in air, at 800 °C) $S_3^{\bullet-}$ is the most stable sulfide species. Annealing of the preheated samples in air at 800 °C results in partial reverse transformations: $S_2^{\bullet-} + S^{2-} + 2O_2(\text{gas}) \rightarrow SO_4^{2-}$, $S_4^{\bullet-} + S_2^{\bullet-} \rightarrow 2S_3^{\bullet-}$, as well as subordinate processes $S_3^{\bullet-} + 5e + 6O_2(\text{gas}) \rightarrow 3SO_4^{2-}$ and $C_2O_4^{2-} \rightarrow 2CO_2(\text{gas}) + 2e$. The oxidation of $S_3^{\bullet-}$ into SO_4^{2-} can proceed only partly due to the charge-balance requirement.

As noted above, $S_3^{\bullet-}$ is a very strong blue chromophore and even trace amounts of this radical anion are detectable by Raman spectroscopy. However, $S_3^{\bullet-}$ was not detected in sapozhnikovite. The possible cause of this fact is a high concentration of lithium in peralkaline rocks of the Lovozero massif (55 ppm, in average [66], whereas, e.g., in peralkaline rocks of the Khibiny massif, the mean Li content is only 20 ppm). Unlike other metal cations, Li^+ reacts with $S_3^{\bullet-}$ to form a cyclic radical anion $LiS_3^{\bullet}$ with strong covalent Li–S bonds [67], which results in the immobilization of $S_3^{\bullet-}$. Kyanoxalite containing trace

amounts of $S_3^{\bullet-}$ crystallized after sapozhnikovite at the hydrothermal zeolite stage with a lowered activity of lithium and containing trace amounts of $S_3^{\bullet-}$ [58].

4.3. Color Centers in Sodalite-group Minerals

Sodalite-group minerals show a wide range of colors. In particular, yellow, pink, violet, lilac, green, and blue samples are known. In most cases, coloration of sodalite-group minerals is caused by S-bearing extra-framework components. The $S_3^{\bullet-}$ radical anion is a very strong chromophore [45] which causes the deep blue color of lazurite [5]. Blue color of haüyne is usually due to trace amounts of $S_3^{\bullet-}$ [3,4,44,48]. The main yellow chromophore in sodalite-group minerals is the $S_2^{\bullet-}$ radical anion, which occurs in significant amounts in yellow varieties of bolotinaite (IMA 2021-088) earlier described as an "F-rich sodalite-group mineral" [4] as well as in above-described yellow products of heating of haüyne under reducing conditions.

Green chromophores are unknown among extra-framework components in sodalite-group minerals. Green color of some varieties of haüyne and slyudyankaite appears as a result of the presence of both $S_3^{\bullet-}$ and a yellow chromophore ($S_2^{\bullet-}$ and/or S_6). However, S_6 is a rather weak chromophore [41].

Pink color of sodalite-group minerals (in particular, sodalite and tugtupite) may have different causes, including the presence of S_4 or $S_4^{\bullet-}$ [41,45], Cr^{3+} or F-centers [68]. Lilac and violet tints of some haüyne samples from gem lazutite deposits (Sample 1 in this work; see [3,4]) is due to simultaneous presence of S_4 or $S_4^{\bullet-}$ and trace amounts of $S_3^{\bullet-}$.

Color coordinates in the CIE1931 color space chromaticity diagram for the samples studied in this work using NIR/Vis/UV spectroscopy are shown in Figure 22. Coordinates of coloration were calculated for daylight illuminant D with 4500 K temperature.
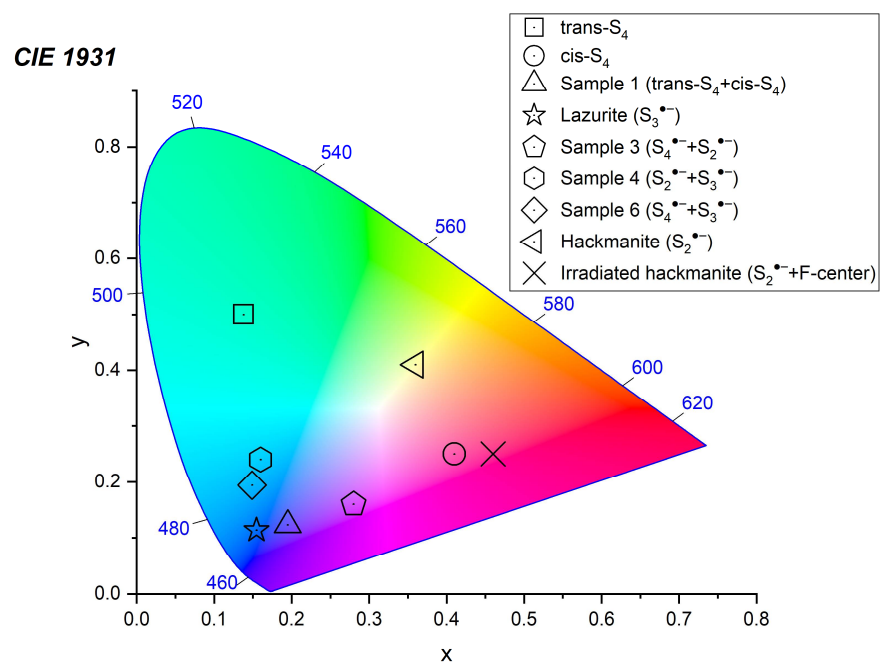
Figure 22. Color space chromaticity diagram for sodalite-group minerals.

Lilac-blue color of Sample 1 may be partly due to the presence of two conformers of S_4 that absorb mainly in the middle part of the visible range with band maximums shifted in opposite directions (towards blue and red ranges). However, the Raman spectrum of Sample 1 shows a series of characteristic bands of the $S_3^{\bullet-}$ radical anion, which may be an additional cause of the blue tint.

The color change of hackmanite and tugtupite upon irradiation with ultraviolet light from colorless or pale pink to purple is explained by the transfer of an electron from the impurity S_2^{2-} anions to the Cl vacancy, with the formation of color centers (F-centers). The

absorption band of the F-centers is located at about 550 nm. The resulting $S_2^{\bullet-}$ radical anions practically do not affect the color due to their low concentration and relatively low oscillator strength. When irradiated with visible light, the F-centers disappear due to the phototransfer of an electron back to $S_2^{\bullet-}$, and the crystals become colorless. This reversible color change is called tenebrescence or photochromism. It is noteworthy that the presence of significant amounts of potassium in the mineral leads to the disappearance of photochromism: in hackmanite and tugtupite, where sodium sharply predominates among the extraframework cations, photochromism is observed, unlike haüyne, despite hauine usually containing a fairly large number of $S_2^{\bullet-}$ centers. The causes of this are still being discussed. Perhaps this phenomenon is due to the fact that when sodium is replaced by potassium, either the value of the energy barrier for electron phototransfer from sulfur to a vacancy changes, or the excited state of the F-center enters the conduction band. Radiation coloring of haüyne does not change the visible color caused by F-centers. The presence of Fe^{3+} and Ti^{3+} impurities also affects the intensity of photochromic color and luminescence of $S_2^{\bullet-}$ radical anions [69].

Other possible radical anions in minerals of the sodalite group are $SO_4^{\bullet-}$ и $SO_3^{\bullet-}$. The most intense absorption band of $SO_4^{\bullet-}$ is located at about 450 nm and the second band is at about 300 nm in $Na_2S_2O_8$ [70]. It was noted in [71] that there is an electron transfer between Fe^{2+} и $SO_4^{\bullet-}$ with the formation of Fe^{3+} и SO_4^{2-}. Thus, the presence of $SO_4^{\bullet-}$ in the mineral can lead to the loss of the blue color. The radical anion $SO_3^{\bullet-}$ absorbs in the region of about 280 nm and does not affect the color [70].

5. Conclusions

Application of a complex of spectroscopic methods to sodalite-group minerals and products of their thermal conversions made it possible to identify various S- and C-bearing extra-framework components, including SO_4^{2-}, HS^-, S^{2-}, CO_3^{2-}, $C_2O_4^{2-}$, $HC_2O_4^-$, Cl^-, and F^- anions $S_2^{\bullet-}$, $S_3^{\bullet-}$, $S_4^{\bullet-}$, and $S_6^{\bullet-}$ radical anions as well as CO_2, H_2O, and S_4 neutral molecules. The composition of extra-framework species in sodalite-group minerals may serve as a marker of mineral-forming media including fugacities of volatile components (H_2O, O_2, CO_2, HF, SO_2, and polysulfide compounds). Complex mutual transformations of these components are observed during heating at high temperatures. The scheme of transformations of extra-framework components in SO_4^{2-}-bearing members of the sodalite group during their heating at 700 °C under reducing conditions includes the elementary processes $SO_4^{2-} \rightarrow S^{2-} + 2O_2(gas)$, $CO_2 + 2SO_4^{2-} + H_2O \rightarrow 2HS^- + CO_3^{2-} + 4O_2(gas)$. $3SO_4^{2-} \rightarrow S_3^{\bullet-} + 5e + 6O_2(gas)$, $2S_3^{\bullet-} \rightarrow S_2^{\bullet-} + S_4^{\bullet-}$, and $2CO_2 + 2e \rightarrow C_2O_4^{2-}$ (e = electron). Subsequent annealing in air at 800 °C results in the partial reverse transformations $S_2^{\bullet-} + S^{2-} + 2O_2(gas) \rightarrow SO_4^{2-}$, $S_4^{\bullet-} + S_2^{\bullet-} \rightarrow 2S_3^{\bullet-}$, $S_3^{\bullet-} + 5e + 6O_2(gas) \rightarrow 3SO_4^{2-}$, and $C_2O_4^{2-} \rightarrow 2CO_2(gas) + 2e$.

Based on these data, it can be concluded that natural HS^-- and CO_2^0-bearing sodalite-group minerals can be formed under reducing conditions and as a result of thermal transformation of an initial mineral, respectively. In this respect, the occurrence of the HS^--dominant mineral sapozhnikovite in association with the oxalate-rich cancrinite-type mineral kyanoxalite in agpaitic rocks [58] and the occurrence of a CO_3^{2-}-bearing sodalite-group mineral in a metasomatic volcanic ejectum [65] are indicative.

Normally, the oxalate group is unstable at temperatures higher than 500 °C. However, it was shown that the occurrence of oxalate anions in wide channels of cancrinite-group minerals is a stabilizing factor. In particular, oxalate anions in kyanoxalite decompose at 700 °C [72]. New data obtained in this work show that oxalate groups in sodalite cages are relatively stable up to 700 °C and decompose at 800 °C. Earlier we have shown that similar stabilization of nitrate anion takes place in cancrinite channels [73].

Color variations of sodalite-group minerals are mainly caused by the presence of S-bearing chromophores, $S_3^{\bullet-}$ (blue), $S_2^{\bullet-}$ and/or S_6 (yellow), $S_4^{\bullet-}$ and/or S_4 (red). Green color is due to the simultaneous presence of blue and yellow chromophores.

References

1. Baerlocher, C.; McCusker, L.B. Database of Zeolite Structures, (n.d.). Available online: http://www.iza-structure.org/databases/ (accessed on 16 June 2022).

2. Fischer, R.X.; Baur, W.H. Symmetry relationships of sodalite (SOD)-type crystal structures. *Z. Krist.* **2009**, *224*, 185–197. [CrossRef]

3. Chukanov, N.V.; Vigasina, M.F.; Zubkova, N.V.; Pekov, I.V.; Schäfer, C.; Kasatkin, A.V.; Yapaskurt, V.O.; Pushcharovsky, D.Y. Extra-framework content in sodalite-group minerals: Complexity and new aspects of its study using infrared and Raman spectroscopy. *Minerals* **2020**, *10*, 363. [CrossRef]

4. Chukanov, N.V.; Sapozhnikov, A.N.; Shendrik, R.Y.; Vigasina, M.F.; Steudel, R. Spectroscopic and crystal-chemical features of sodalite-group minerals from gem lazurite deposits. *Minerals* **2020**, *10*, 1042. [CrossRef]

5. Sapozhnikov, A.N.; Chukanov, N.V.; Shendrik, R.Y.; Vigasina, M.F.; Tauson, V.L.; Lipko, S.V.; Belakovskiy, D.I.; Levitskiy, V.I.; Suvorova, L.F.; Ivanova, L.A. Lazurite: Confirmation of the status as a mineral species with the formula $Na_7Ca(Al_6Si_6O_{24})(SO_4)$ $S_3^{\bullet-}\cdot H_2O$ and new data. *Zap. Ross. Mineral. Obs. (Proc. Russ. Mineral Soc.)* **2021**, *150*, 92–102. [CrossRef]

6. Shchipalkina, N.V.; Pekov, I.V.; Koshlyakova, N.N.; Britvin, S.N.; Zubkova, N.V.; Varlamov, D.A.; Sidorov, E.G. Unusual silicate mineralization in fumarolic sublimates of the Tolbachik volcano, Kamchatka, Russia—Part 2: Tectosilicates. *Eur. J. Mineral.* **2020**, *32*, 121–136. [CrossRef]

7. Chukanov, N.V.; Aksenov, S.M.; Rastsvetaeva, R.K. Structural chemistry, IR spectroscopy, properties, and genesis of natural and synthetic microporous cancrinite- and sodalite-related materials: A review. *Micropor. Mesopor. Mater.* **2021**, *323*, 111098. [CrossRef]

8. Gobeltz-Hautecoeur, N.; Demortier, A.; Lede, B.; Lelieur, J.P.; Duhayon, C. Occupancy of the sodalite cages in the blue ultramarine pigments. *Inorg. Chem.* **2002**, *41*, 2848–2854. [CrossRef]

9. Heil, C.; Cataldo, S.; Bachelet, G.B.; Boeri, L. Superconductivity in sodalite-like yttrium hydride clathrates. *Phys. Rev. B Condens. Matter.* **2019**, *99*, 220502(R). [CrossRef]

10. Ogura, M.; Morozumi, K.; Elangovan, S.P.; Tanada, H.; Ando, H.; Okubo, T. Potassium-Doped sodalite: A tectoaluminosilicate for the catalytic material towards continuous combustion of carbonaceous matters. *Appl. Catal. B* **2008**, *77*, 294–299. [CrossRef]

11. Shanbhag, G.V.; Choi, M.; Kim, J.; Ryoo, R. Mesoporous sodalite: A novel, stable solid catalyst for base-catalyzed organic transformations. *J. Catal.* **2009**, *264*, 88–92. [CrossRef]

12. Sachse, A.; Galarneau, A.; Renzo, F.D.; Fajula, F.; Coq, B. Synthesis of zeolite monoliths for flow continuous processes. The case of sodalite as a basic catalyst. *Chem. Mater.* **2010**, *22*, 4123–4125. [CrossRef]

13. Hiyoshi, N. Nanocrystalline sodalite: Preparation and application to epoxidation of 2-cyclohexen-1-one with hydrogen peroxide. *Appl. Catal.* **2012**, *419–420*, 164–169. [CrossRef]

14. Manique, M.C.; Lacerda, L.V.; Alves, A.K.; Bergmann, C.P. Biodiesel production using coal fly ash-derived sodalite as a heterogeneous catalyst. *Fuel* **2017**, *190*, 268–273. [CrossRef]

15. Wang, S.; Zhao, Z.-J.; Chang, X.; Zhao, J.; Tian, H.; Yang, C.; Li, M.; Fu, Q.; Mu, R.; Gong, J. Activation and spillover of hydrogen on sub-1 nm palladium nanoclusters confined within sodalite zeolite for the semi-hydrogenation of alkynes. *Angew. Chem. Int. Ed.* **2019**, *58*, 7668–7672. [CrossRef]

16. Khajavi, S.; Jansen, J.C.; Kapteijn, F. Production of ultra pure water by desalination of seawater using a hydroxyl sodalite membrane. *J. Membr. Sci.* **2010**, *356*, 52–57. [CrossRef]

17. Nabavi, M.S.; Mohammadi, T.; Kazemimoghadam, M. Hydrothermal synthesis of hydroxyl sodalite zeolite membrane: Separation of H_2/CH_4. *Ceram. Int.* **2014**, *40*, 5889–5896. [CrossRef]

18. Kalantari, N.; Vaezi, M.J.; Yadollahi, M.; Babaluo, A.A.; Bayati, B.; Kazemzadeh, A. Synthesis of nanostructure hydroxysodalite composite membranes via hydrothermal method: Support surface modification and synthesis method effects. *Asia-Pac. J. Chem. Eng.* **2015**, *10*, 45–55. [CrossRef]

19. Wei, X.-L.; Pan, W.-Y.; Li, X.; Pan, M.; Huo, C.-F.; Yang, R.; Chao, Z.-S. MCM-22 zeolite-induced synthesis of thin sodalite zeolite membranes. *Chem. Mater.* **2020**, *32*, 333–340. [CrossRef]

20. Yang, G.; Guo, H.; Kang, Z.; Feng, S.; Zhao, L.; Mintova, S. Sandwich-type H_2/CO_2 membranes comprising of graphene oxide and sodalite crystals with adjustable morphology and size. *Micropor. Mesopor. Mater.* **2020**, *300*, 110120. [CrossRef]

21. Eterigho-Ikelegbe, O.; Bada, S.O.; Daramola, M.O. Preparation and evaluation of nanocomposite sodalite/α-Al_2O_3 tubular membranes for H_2/CO_2 separation. *Membranes* **2020**, *10*, 312. [CrossRef]

22. Eden, C.L.; Daramola, M.O. Evaluation of silica sodalite infused polysulfone mixed matrix membranes during H_2/CO_2 separation. *Mater. Today Proc.* **2021**, *38*, 522–527. [CrossRef]

23. Ntshangase, N.C.; Sadare, O.O.; Daramola, M.O. Effect of silica sodalite functionalization and PVA coating on performance of sodalite infused PSF membrane during treatment of acid mine drainage. *Membranes* **2021**, *11*, 315. [CrossRef] [PubMed]

24. Navarro, J.A.R.; Barea, E.; Salas, J.M.; Masciocchi, N.; Galli, S.; Sironi, A.; Ania, C.O.; Parra, J.B. H_2, N_2, CO, and CO_2 sorption properties of a series of robust sodalite-type microporous coordination polymers. *Inorg. Chem.* **2006**, *45*, 2397–2399. [CrossRef] [PubMed]

25. Asgari, A.; Jawahery, S.; Bloch, E.D.; Hudson, M.R.; Flacau, R.; Vlaisavljevich, B.; Long, J.R.; Brown, C.M.; Queen, W.L. An experimental and computational study of CO_2 adsorption in the sodalite-type *M*-BTT (*M* = Cr, Mn, Fe, Cu) metal–organic frameworks featuring open metal sites. *Chem. Sci.* **2018**, *9*, 4579–4588. [CrossRef]

26. Wang, Y.; Jiang, Y.; Hu, S.; Peng, S.; Xu, C.; Lu, A. Dehydrated $Na_6[AlSiO_4]_6$ sodalite as a promising SO_2 sorbent material: A first principles thermodynamics prediction. *J. Amer. Ceram. Soc.* **2019**, *102*, 3663–3672. [CrossRef]

27. Asgari, M.; Semino, R.; Schouwink, P.A.; Kochetygov, I.; Tarver, J. Understanding how ligand functionalization influences CO_2 and N_2 adsorption in a sodalite metal-organic framework. *Chem. Mater.* **2020**, *32*, 1526–1536. [CrossRef]

28. Dickson, J.O.; Harsh, J.B.; Lukens, W.W.; Pierce, E.M. Perrhenate incorporation into binary mixed sodalites: The role of anion size and implications for technetium-99 sequestration. *Chem. Geol.* **2015**, *395*, 138–143. [CrossRef]

29. Gilbert, M.R. Pressureless sintering of sodalite waste-forms for the immobilization of pyroprocessing wastes. In *MRS Online Proceedings Library (OPL): Symposium EE—Scientific Basis for Nuclear Waste Management XXXVIII*; Cambridge University Press: cambrige, UK, 2015; Volume 1744, pp. 61–66. [CrossRef]

30. Luksic, S.A.; Riley, B.J.; Parker, K.E.; Hrma, P. Sodalite as a vehicle to increase Re retention in waste glass stimulant during vitrification. *J. Nucl. Mater.* **2016**, *479*, 331–337. [CrossRef]

31. Vance, E.R.; Gregg, D.J.; Grant, C.; Stopic, A.; Maddrell, E.R. Silver iodide sodalite for [129]I immobilization. *J. Nucl. Mater.* **2016**, *480*, 177–181. [CrossRef]

32. Lilova, K.; Pierce, E.M.; Wu, L.; Jubb, A.M.; Subramani, T.; Navrotsky, A. Energetics of salt-bearing sodalites, $Na_8Al_6Si_6O_{24}X_2$ (*X* = SO_4, ReO_4, Cl, I): A treatment option for pertechnetate-enriched nuclear waste streams. *ACS Earth Space Chem.* **2020**, *4*, 2153–2161. [CrossRef]

33. Grajciar, L. PbS clusters embedded in sodalite zeolite cavities of different compositions: Unraveling the structural evolution and optical properties using ab initio calculations. *J. Phys. Chem.* **2016**, *C120*, 27050–27065. [CrossRef]

34. Van den Berg, A.W.C.; Bromley, S.T.; Jansen, J.C. Thermodynamic limits on hydrogen storage in sodalite framework materials: A molecular mechanics investigation. *Micropor. Mesopor. Mater.* **2005**, *78*, 63–71. [CrossRef]

35. Zheng, Z.; Guliants, V.V.; Misture, S. Sodalites as ultramicroporous frameworks for hydrogen separation at elevated temperatures: Thermal stability, template removal, and hydrogen accessibility. *J. Porous Mater.* **2009**, *16*, 343–347. [CrossRef]

36. Rüscher, C.H.; Stemme, F.; Schomborg, L.; Buhl, J.-C. Low temperature hydrogen release from borontetrahydride-sodalite and its reloading: Observations in in situ and ex situ TIR experiments. In *Ceramics for Environmental and Energy Applications*; Boccaccini, A., Marra, J., Dogan, F., Lin, H.-T., Watanabe, T., Eds.; John Wiley & Sons, Inc.: Hoboken, NJ, USA, 2010; pp. 65–70.

37. Gong, Y.-N.; Meng, M.; Zhong, D.-C.; Huang, Y.-L.; Jiang, L.; Lu, T.-B. Counter-Cation modulation of hydrogen and methane storage in a sodalite-type porous metal–organic framework. *Chem. Commun.* **2012**, *48*, 12002–12004. [CrossRef]

38. Sapozhnikov, A.N.; Bolotina, N.B.; Chukanov, N.V.; Kaneva, E.V.; Shendrik, R.Y.; Vigasina, M.F.; Ivanova, L.A. IMA Commission on New Minerals, Nomenclature and Classification (CNMNC)—Newsletter 65. *Eur. J. Mineral.* **2022**, *34*, 143–148. [CrossRef]

39. Chukanov, N.V.; Zubkova, N.V.; Pekov, I.V.; Shendrik, R.Y.; Varlamov, D.A.; Vigasina, M.F.; Belakovskiy, D.I.; Britvin, S.N.; Yapaskurt, V.O.; Pushcharovsky, D.Y. Sapozhnikovite, $Na_8(Al_6Si_6O_{24})(HS)_2$, a new sodalite-group mineral from the Lovozero alkaline massif, Kola Peninsula. *Mineral. Mag.* **2022**, *86*, 49–59. [CrossRef]

40. Rejmak, P. Computational refinement of the puzzling red tetrasulfur chromophore in ultramarine pigments. *Phys. Chem. Chem. Phys.* **2020**, *22*, 22684–22698. [CrossRef]

41. Eckert, B.; Steudel, F. Molecular spectra of sulfur molecules and solid sulfur allotropes. *Top. Curr. Chem.* **2003**, *231*, 31–97. [CrossRef]

42. Hettmann, K.; Wenzel, T.; Marks, M.; Markl, G. The sulfur speciation in S-bearing minerals: New constraints by a combination of electron microprobe analysis and DFT calculations with special reference to sodalite-group minerals. *Amer. Mineral.* **2012**, *97*, 1653–1661. [CrossRef]

43. Ling, Z.C.; Wang, A.; Jolliff, B.L. Mineralogy and geochemistry of four lunar soils by laser-Raman study. *Icarus* **2011**, *211*, 101–113. [CrossRef]

44. Sapozhnikov, A.N.; Tauson, V.L.; Lipko, S.V.; Shendrik, R.Y.; Levitskii, V.I.; Suvorova, L.F.; Chukanov, N.V.; Vigasina, M.F. On the crystal chemistry of sulfur-rich lazurite, ideally $Na_7Ca(Al_6Si_6O_{24})(SO_4)(S_3)^-\cdot nH_2O$. *Amer. Mineral.* **2021**, *106*, 226–234. [CrossRef]

45. Steudel, R. Inorganic polysulfides S_n^{2-} and radical anions $S_n^{\bullet-}$. In *Elemental Sulfur und Sulfur-Rich Compounds II. Topics in Current Chemistry*; Steudel, R., Ed.; Springer: Berlin/Heidelberg, Germany, 2003; Volume 231.

46. Steudel, R.; Chivers, T. The role of polysulfide dianions and radical anions in the chemical, physical and biological sciences, including sulfur-based batteries. *Chem. Soc. Rev.* **2019**, *48*, 3279–3319 and 4338. [CrossRef]

47. Wong, M.W.; Steudel, R. Structure and spectra of tetrasulfur S_4—An ab initio MO study. *Chem. Phys. Lett.* **2003**, *379*, 162–169. [CrossRef]

48. Caggiani, M.C.; Mangone, A.; Aquafredda, P. Blue coloured haüyne from Mt. Vulture (Italy) volcanic rocks: SEM-EDS and Raman investigation of natural and heated crystals. *J. Raman Spectrosc.* **2022**, *53*, 956–968. [CrossRef]

49. Bény, C.; Guilhaumou, N.; Touray, J.-C. Native-Sulphur-Bearing fluid inclusions in the CO_2-H_2S-H_2O-S system—Microthermometry and Raman microprobe (MOLE) analysis—Thermochemical interpretations. *Chem. Geol.* **1982**, *37*, 113–127. [CrossRef]

50. Dubessy, J.; Boiron, M.-C.; Moissette, A.; Monnion, C.; Sretenskaya, N. Determination of water, hydrates and pH in fluid inclusions by micro-Raman spectrometry. *Eur. J. Mineral.* **1992**, *4*, 885–894. [CrossRef]

51. Kaneva, E.; Shendrik, R.; Mesto, E.; Bogdanov, A.; Vladykin, N. Spectroscopy and crystal chemical properties of $NaCa_2[Si_4O_{10}]F$ natural agrellite with tubular structure. *Chem. Phys. Lett.* **2020**, *738*, 136868. [CrossRef]

52. Weser, G.; Hensel, F.; Warren, W.W. The optical absorption spectrum of fluid sulfur up to supercritical conditions. *Ber. Bunsenges. Phys. Chem.* **1978**, *82*, 588–594. [CrossRef]

53. Paniz, H.; Lester, A. Vibronic absorption spectra of S3 and S4, in solid argon. *J. Phys. Chem.* **1992**, *96*, 6579–6585.

54. Annersten, H.; Haseeb, A. Blue sodalite. *Canad. Mineral.* **1979**, *17*, 39–46.

55. Radomskaya, T.A.; Kaneva, E.V.; Shendrik, R.Y.; Suvorova, L.F.; Vladykin, N.V. Sulfur-Bearing sodalite, hackmanite, in alkaline pegmatites of the Inagli massif (Aldan Shield): Crystal chemistry, photochromism, and luminescence. *Geol. Ore Depos.* **2021**, *63*, 696–704. [CrossRef]

56. Tauson, V.L.; Akimov, V.V.; Sapozhnikov, A.N.; Kuznetzov, K.E. Investigation of the stability conditions and structural-chemical transformations of Baikal lazurite. *Geochem. Int.* **1998**, *36*, 717–733.

57. Rastsvetaeva, R.K.; Sapozhnikov, A.N.; Tauson, V.L.; Kashaev, A.A. Crystal structure of sulfide sodalite, a product of sulfate sulfur reduction in lazurite. *Dokl. Akad. Nauk.* **1997**, *356*, 773–776. (In Russian)

58. Chukanov, N.V.; Vigasina, M.F.; Shendrik, R.Y.; Varlamov, D.A.; Pekov, I.V.; Zubkova, N.V. Nature and Isomorphism of Extra-Framework Components in cancrinite- and sodalite-related minerals: New data. *Minerals* **2022**, *12*, 729. [CrossRef]

59. Steudel, R.; Jensen, D.; Göbel, P.; Hugo, P. Optical absorption spectra of the homocyclic sulfur molecules S_n (n = 6, 7, 8, 9, 10, 12, 15, 20) in solution. *Ber. Bunsenges. Phys. Chem.* **1988**, *92*, 118–122. [CrossRef]

60. Raulin, K.; Gobeltz, N.; Vezin, H.; Touat, N.; Ledé, B.; Moissette, A. Identification of the EPR signal of S_2^- in green ultramarine pigments. *Phys. Chem. Chem. Phys.* **2011**, *13*, 9253–9259. [CrossRef]

61. Pokrovski, G.S.; Dubrovinsky, L.S. The S_3^- ion is stable in geological fluids at elevated temperatures and pressures. *Science* **2011**, *331*, 1052–1054. [CrossRef]

62. Pokrovski, G.S.; Dubessy, J. Stability and abundance of the trisulfur radical ion S_3^- in hydrothermal fluids. *Earth Planet. Sci. Lett.* **2015**, *411*, 298–309. [CrossRef]

63. Arieli, D.; Vaughan, D.E.W.; Goldfarb, D. New synthesis and insight into the structure of blue ultramarine pigments. *J. Amer. Chem. Soc.* **2004**, *126*, 5776–5788. [CrossRef]

64. Ostroumov, M.; Fritsch, E.; Faulques, E.; Chauvet, O. Etude spectrometrique de la lazurite du Pamir, Tajikistan. *Canad. Mineral.* **2002**, *40*, 885–893. [CrossRef]

65. Ballirano, O.; Maras, A. Crystal chemical and structural characterization of an unusual CO_3-bearing sodalite-group mineral. *Eur. J. Mineral.* **2005**, *17*, 805–812. [CrossRef]

66. Gerasimovskiy, V.I.; Volkov, V.P.; Kogarko, L.N.; Polyalov, A.I.; Saprykina, T.V.; Balashov, Y.A. *Geochemistry of the Lovozero Alkaline Massif*; Nauka: Moskow, Russia, 1966. (In Russian)

67. Zhang, B.; Wu, J.; Gu, J.; Li, S.; Yan, T.; Gao, X.-P. The fundamental understanding of lithium polysulfides in ether-based electrolyte for lithium-sulfur batteries. *ACS Energy Lett.* **2021**, *6*, 537–546. [CrossRef]

68. Finch, A.A.; Friis, H.; Maghrabi, M. Defects in sodalite-group minerals determined from X-ray-induced luminescence. *Phys. Chem. Miner.* **2016**, *43*, 481–491. [CrossRef]

69. Agamah, C.; Vuori, S.; Colinet, P.; Norrbo, I.; Miranda de Carvalho, J.; Key, L.; Nakamura, O.; Lindblom, J.; van Goethem, L.; Emmermann, A.; et al. Hackmanite—The natural glow-in-the-dark material. *Chem. Mater.* **2020**, *32*, 8895–8905. [CrossRef]

70. Huie, R.E.; Clifton, C.L.; Altstein, N. A pulse radiolysis and flash photolysis study of the radicals SO_2^-, SO_3^-, SO_4^- and SO_5^-. *Int. J. Radiat. Appl. Instr. Part C Radiat. Phys. Chem.* **1989**, *33*, 361–370. [CrossRef]

71. McElroy, W.J.; Waygood, S.J. Kinetics of the reactions of the SO_4^- radical with SO_4^-, $S_2O_8^{2-}$, H_2O and Fe^{2+}. *J. Chem. Soc. Faraday Trans.* **1990**, *86*, 2557. [CrossRef]

72. Olysych, L.V.; Vigasina, M.F.; Melchakova, L.V.; Pekov, I.V.; Chukanov, N.V. Study of thermal decomposition of the cancrinite-kyanoxalite solid-solution series minerals. In Proceedings of the Abstracts of XXVII International Conference "Geochemistry of Magmatic Rocks", Moscow, Russia, 9–16 September 2010; pp. 135–136.

73. Chukanov, N.V.; Zubkova, N.V.; Buhl, J.-C.; Pekov, I.V.; Ksenofontov, D.A.; Depmeier, W.; Pushcharovskii, D.Y. Crystal structure of nitrate cancrinite synthesized under low-temperature hydrothermal conditions. *Dokl. Earth Sci.* **2011**, *438*, 669–672. [CrossRef]